

# Chapter 3

## Free Rotating Disk

### 3.1 Laminar Flow

A flow and heat transfer pattern over a single rotating disk is schematically depicted in Fig. 2.1. Self-similar velocity and temperature profiles,  $F_0$ ,  $G_0$ ,  $H_0$  and  $\theta$ , computed numerically using the Mathcad software as a solution of Eqs. (2.32)–(2.36) for  $\beta = 0$ ,  $N = 0$  [1] agree well with computations [2–5] and experiments [6–8] (Fig. 3.1). Derivatives of the  $F_0$  and  $G_0$  profiles at the disk wall, as well as the mass flow rate in the boundary layer are given by the following relations [3, 4]

$$G'_{0w} = (dG_0/d\zeta_0)_{\zeta=0} = -0.6159, \quad F'_{0w} = (dF_0/d\zeta_0)_{\zeta=0} = 0.5102, \quad (3.1)$$

$$\alpha_0 = -F'_{0w}/G'_{0w} = 0.8284, \quad \dot{m}_d/(\mu r) = 0.8845Re_\omega^{1/2}. \quad (3.2)$$

In laminar flow, the boundary layer over a rotating disk has a constant thickness  $\delta_0$ . Assuming  $G_0 = 0.01$  at the outer edge of the boundary layer, one can obtain  $\delta_0 = 5.5(\omega/\nu)^{1/2}$  [3]. The numerical coefficient is higher for smaller values of  $G_0$  defining the location of  $\delta_0$ , which, however, is unimportant in the integral method approach [1, 3].

For a single rotating disk, the moment coefficient of  $C_M$  is given by [2]

$$C_M = 3.87Re_\omega^{-1/2}. \quad (3.3)$$

Equation (3.3) agrees with experiments [9] and differs modestly from the data [10, 11] (Fig. 3.2), which might be attributed to a poorer accuracy of the measurements.

Generally, the heat transfer rate over rotating disks follows the relations

$$Nu = K_1Re_\omega^{n_R}, \quad Nu_{av} = K_2Re_\omega^{n_R}. \quad (3.4)$$

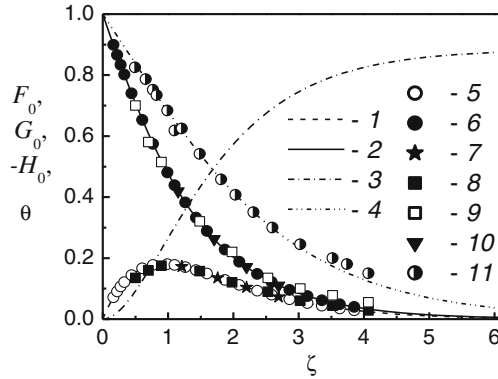


**Fig. 3.1** Velocity and temperature profiles in laminar flow over a free rotating disk [1]. Computations: 1— $F_0$ , 2— $G_0$ , 3— $(-H_0)$ , 4— $\theta$  for  $n_* = 0$ ,  $Pr = 0.71$ . Experiments: 5— $F_0$  [7], 6— $F_0$  [6], 7— $F_0$  [8], 8— $G_0$  [7], 9— $G_0$  [6], 10— $G_0$  [8], 11— $\theta$  for  $n_* = 0$ ,  $Pr = 0.71$  [6]. Subscript “0”: a free disk

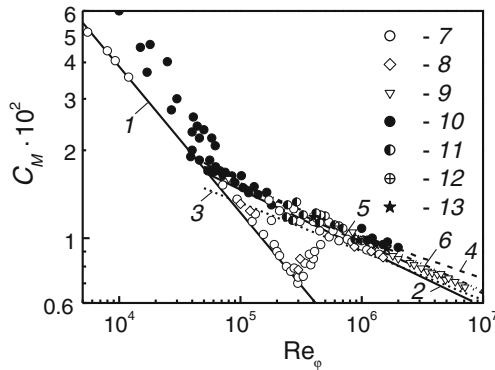


**Fig. 3.2** Moment coefficient of a free rotating disk [1]. Laminar flow: 1—Eq. (3.3). Turbulent flow: 2—Eq. (2.80),  $n = 1/7$ ; 3—(2.80),  $1/9$ ; 4—(3.18); 5—(3.19), 6—(3.20). Experiments: 7, 8, 9—[9], 10—[10], 11—[11], 12—[12], 13—[13]. Data 7–11 cited according to [2, 5]; data [12, 13] processed in [14]. Subscript “0”: a free disk

Flow regime, Prandtl number and function of the wall temperature determine coefficients  $K_1$  and  $K_2$  in Eq. (3.4). The constant  $n_R$  is determined by the flow regime. For instance,  $K_1 = K_2$ ,  $n_R = 1/2$  in laminar flow [2–4, 6]. For an isothermal rotating disk at  $Pr = 0.71–0.72$  (air), the most reliable experiments yield  $K_1 = 0.32–0.34$  [3, 4, 6, 15–25] (Fig. 3.3).

Values of the constant  $K_1$  obtained by the author [1] are presented in Table 3.1.

They result from a solution of Eqs. (2.32)–(2.36) for  $\beta = 0$ ,  $N = 0$  under condition (2.30)

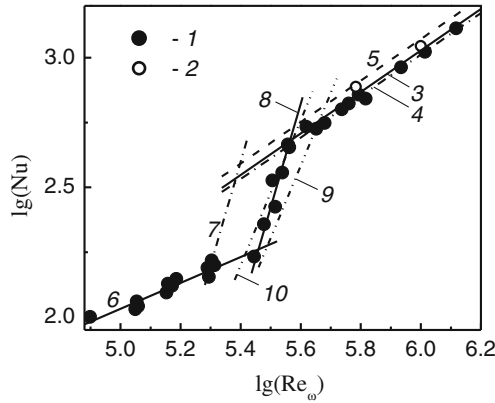


**Fig. 3.3** Local Nusselt numbers on a rotating disk [1]. Experiments [6]: 1— $l-q_w = \text{const.}$ ; 2— $T_w \approx \text{const.}$  3–10—calculations, Eq. (3.4). Turbulent flow,  $n_R = 0.8$ : 3— $K_1 = 0.0169$  [26]; 4— $K_1 = 0.0163$  [6]; 5— $K_1 = 0.0187$  [26]. Laminar flow,  $n_R = 0.5$ : 6— $K_1 = 0.34$  [6]. Transitional flow: 7— $n_R = 4$ ,  $K_1 = 10.0 \times 10^{-20}$  [23]; 8— $n_R = 4$ ,  $K_1 = 2.65 \times 10^{-20}$  [6]; 9— $n_R = 2.8$ ,  $K_1 = 8.01 \times 10^{-14}$  [27, 28]; 10— $n_R = 2.8$ ,  $K_1 = 1.2 \times 10^{-13}$  [1]

**Table 3.1** Constant  $K_1$  according to the exact solution of Eqs. (2.32)–(2.36) [1, 29, 30]

$Pr$	$n_* = -2$	$n_* = -1.5$	$n_* = -1$	$n_* = -0.5$	$n_* = 0$	$n_* = 1$	$n_* = 2$	$n_* = 3$	$n_* = 4$
1.0	0.0	0.1305	0.2352	0.3221	0.3963	0.5180	0.6159	0.6982	0.7693
0.9	0.0	0.1217	0.2204	0.3029	0.3737	0.4905	0.5849	0.6643	0.7331
0.8	0.0	0.1124	0.2046	0.2824	0.3495	0.4608	0.5513	0.6276	0.6939
0.72	0.0	0.1045	0.1911	0.2647	0.3286	0.4352	0.5223	0.5959	0.6599
0.71	0.0	0.1035	0.1893	0.2624	0.3259	0.4319	0.5185	0.5918	0.6555
0.6	0.0	0.0917	0.1691	0.2358	0.2943	0.3929	0.4742	0.5433	0.6036
0.5	0.0	0.0802	0.1490	0.2091	0.2623	0.3531	0.4287	0.4935	0.5502
0.4	0.0	0.0675	0.1267	0.1792	0.2263	0.3078	0.3767	0.4362	0.4887
0.3	0.0	0.0536	0.1017	0.1452	0.1849	0.2550	0.3153	0.3682	0.4153
0.2	0.0	0.0381	0.0732	0.1058	0.1362	0.1912	0.2400	0.2838	0.3234
0.1	0.0	0.0204	0.0399	0.0586	0.0766	0.1104	0.1417	0.1709	0.1981

$$K_1 = -\theta'_{\zeta=0}. \tag{3.5}$$

For  $T_w = \text{const.}$  and  $q_w = \text{const.}$ , the exponent in Eq. (2.30) for laminar flow is the same:  $n_* = 0$ . The constant  $K_1$  is an increasing function of the parameter  $n_*$ : e.g. for air at  $Pr = 0.71$ , the value of  $K_1$  grows up by 313 % with  $n_*$  increasing from  $-1$  to 3 (see Table 3.1). For non-isothermal disks and smaller values of the  $Pr$  number, there are no experimental data in literature that would enable validation of the constant  $K_1$ .

The first known approximate solution valid for gases was derived by Dorfman [2]

$$K_1 = K_2 = 0.308(n_* + 2)^{1/2}Pr^{1/2}. \quad (3.6)$$

Values of  $K_1$  predicted by Eq. (3.6) by 34–238 % surpass the data from Table 3.1 for  $n_* = -1.5-0$ . These deviations are magnified with decreasing  $Pr$  number.

For the conditions of  $T_w = \text{const.}$  and  $Pr = 0-\infty$ , the following theoretical solutions for the constant  $K_1$  were derived in the works [31, 32], respectively

$$K_1 = 0.6109Pr/(0.5301 + 0.3996Pr^{1/2} + Pr)^{2/3}, \quad (3.7)$$

$$K_1 = 0.6Pr/(0.56 + 0.26Pr^{1/2} + Pr)^{2/3}. \quad (3.8)$$

Predictions by Eqs. (3.7) and (3.8) divert from the data in Table 3.1 by maximum 4 and 5 %, accordingly. In the limit at  $Pr \rightarrow 0$ , Eqs. (3.7) and (3.8) tend to a relation  $K_1 \sim Pr$  that conforms to the asymptotic equation  $K_1/Pr = 0.885$  derived in [33]. For  $Pr \rightarrow \infty$ , Eqs. (3.7) and (3.8) reduce to a relation  $K_1 \approx 0.62Pr^{1/3}$ , which coincides with that obtained in the work [33]. Validity of Eqs. (3.7) and (3.8) is restricted by the case of  $n_* = 0$ .

## 3.2 Transition to Turbulent Flow

Increasing the angular velocity of the disk rotation causes instability of laminar flow and set up of spiral vortices followed by a development of turbulence. Authors [34] detected 32 spiral waves over a rotating disk, with the angle  $\varepsilon$  between a perpendicular to the spiral and the radial direction being about  $14^\circ$ . Visualization [35] by means of a thin layer of Kaolin on the surface of a disk revealed simultaneous co-existence of the regions of laminar flow, laminar flow with 28–31 spiral vortices and turbulent flow. The number of spiral vortices is a function of the local Reynolds number  $Re_\omega$  [36–40]. For instance, 14–16 vortices with the angle  $\varepsilon = 20^\circ$  were detected in [37]. The number of vortices  $n_v$  can be predicted by an empirical equation [40]

$$n_v = 0.0698 \cdot Re_\omega^{1/2}. \quad (3.9)$$

Equation (3.9) is confirmed by experimental data [37, 40, 41].

Detailed theoretical investigations of instabilities emerging in flow over a rotating disk were performed in [8, 42–54]. At the onset of instability, the predicted value  $Re_\omega^{1/2} = 286$  conforms to the experimental values [40]. Averaging of the Reynolds number at the onset of transition to turbulent regime yields the value  $Re_\omega^{1/2} = 513$  [42].

Experimental data of different authors summarizing the Reynolds numbers at the onset of instability, beginning and end of transition to turbulent flow are documented in Table 3.2. Table 3.3 lists results of averaging within every sub-group of techniques (heat and mass transfer techniques; thermo-anemometry; visualization and acoustics).

**Table 3.2** Values of the Reynolds number at the onset of instability, beginning and end of transition to turbulent flow [1]

No.	Experimental technique	Values of the Reynolds number $Re_\omega$		
		Onset of instability	Beginning of transition	End of transition
1	Thermoanemometer [34]	$2.1 \times 10^5$		$3.1 \times 10^5$
2	Thermoanemometer [56]	$8.8 \times 10^4$	$2.5 \times 10^5$	$3.2 \times 10^5$
3	Thermoanemometer [40]	$8.6 \times 10^4$	$(2.6-2.8) \times 10^5$	
4	Thermoanemometer [41]	$9 \times 10^4$		$(2.95-3.1) \times 10^5$
5	Thermoanemometer/visualization [57]		$(2.4-2.63) \times 10^5$	
6	Thermoanemometer [38, 39]		$(2.4-2.6) \times 10^5$	
7	Thermoanemometer [8]		$(2.5-2.64) \times 10^5$	
8	Thermoanemometer [7]		$2.5 \times 10^5$	
9	Thermoanemometer [54, 58]	$9.5 \times 10^4$		$3.4 \times 10^5$
10	Acoustic measurements [59]	$1.35 \times 10^5$	$2.55 \times 10^5$	$2.75 \times 10^5$
11	Visualization (Kaolin) [35]	$1.8 \times 10^5$		$3.0 \times 10^5$
12	Visualization (naphthalene) and acoustic measurements [37]	$1.5 \times 10^5$ $(0.33-1.9) \times 10^5$		$2.65 \times 10^5$
13	Visualization in water [60]		$(2.8-2.86) \times 10^5$	$(3.2-4.6) \times 10^5$
14	Heat transfer coefficient [17]	$2.0 \times 10^5$	$2.4 \times 10^5$	
15	Heat transfer coefficient [6]		$2.9 \times 10^5$	$3.6 \times 10^5$
16	Heat transfer coefficient [23]		$1.95 \times 10^5$	$2.5 \times 10^5$
17	Heat transfer coefficient [27, 28]		$2.5 \times 10^5$	$3.2 \times 10^5$
18	Heat transfer coefficient [61]		$2.4 \times 10^5$	
19	Heat transfer coefficient [62]		$2.4 \times 10^5$	
20	Heat transfer coefficient [63]		$2.2 \times 10^5$	$3.4 \times 10^5$
21	Mass transfer coefficient (naphthalene sublimation) [18]		$2.7 \times 10^5$	
22	Mass transfer coefficient (naphthalene sublimation) [16]		$1.9 \times 10^5$	$2.75 \times 10^5$
23	Mass transfer coefficient (naphthalene sublimation) [64]		$1.8 \times 10^5$	
24	Mass transfer coefficient (naphthalene sublimation) [20]		$2.0 \times 10^5$	
25	Mass transfer coefficient (electrochemistry) [42]	$1.7 \times 10^5$	$2.6 \times 10^5$	$3.5 \times 10^5$
26	Mass transfer coefficient (electro-chemistry) [65-67]		$2.3 \times 10^5$	$2.9 \times 10^5$
27	Mass transfer coefficient (electrochemistry) [68]		$2.2 \times 10^5$	$3.0 \times 10^5$

**Table 3.3** Averaged  $Re_\omega$  numbers for boundaries of flow regimes over a rotating disk [1]

No.	Experimental technique	Values of the Reynolds number $Re_\omega$		
		Onset of instability	Beginning of transition	End of transition
1	Thermoanemometer	$1.14 \times 10^5$	$2.54 \times 10^5$	$3.15 \times 10^5$
2	Visualization and acoustic measurements	$1.4 \times 10^5$	$3.08 \times 10^5$	$3.3 \times 10^5$
3	Methods of heat and mass transfer	$1.85 \times 10^5$	$2.3 \times 10^5$	$3.1 \times 10^5$
4	Average value	$1.46 \times 10^5$	$2.64 \times 10^5$	$3.18 \times 10^5$

Different criteria for determining the critical values of  $Re_\omega$  apparently entailed inconsistency of experimental data. In spite of the setup of spiral vortices already for  $Re_\omega = (1.14\text{--}1.4) \times 10^5$ , surface heat and mass transfer rates deviate from the laminar flow data at larger Reynolds numbers  $Re_\omega = 1.85 \times 10^5$ . Also, disagreement between experiments may have been resulted from possible vibrations, different roughness etc. The ratio of the Reynolds numbers at the setup and end of the transition to turbulent flow yields the value 1.21; this agrees with the respective ratio 1.3 for a flat plate flow [55].

The heat/mass transfer rate measured in the transitional flow regime at the same local Reynolds number  $Re_\omega$  was different in various experiments

$$Nu = 10.0 \times 10^{-20} \cdot Re_\omega^4 \quad \text{for } Re_\omega = (1.95\text{--}2.5) \times 10^5 \quad \text{Ref. [23]}, \quad (3.10)$$

$$Nu = 2.65 \times 10^{-20} \cdot Re_\omega^4 \quad \text{for } Re_\omega = (2.9\text{--}3.6) \times 10^5 \quad \text{Ref. [6]}, \quad (3.11)$$

$$Nu = 8.01 \times 10^{-14} \cdot Re_\omega^{2.8} \quad \text{for } Re_\omega = (2.6\text{--}3.2) \times 10^5 \quad \text{Ref. [27, 28]}, \quad (3.12)$$

$$Sh = 20.0 \times 10^{-20} \cdot Re_\omega^4 \quad \text{for } Re_\omega = (2.0\text{--}2.5) \times 10^5 \quad \text{Ref. [16]}, \quad (3.13)$$

$$Sh = 3.4 \times 10^{-14} \cdot Re_\omega^3 Sc^{1/3} \quad \text{for } Re_\omega = (2.0\text{--}3.0) \times 10^5 \quad \text{Ref. [67]}. \quad (3.14)$$

In fact, Eqs. (3.11) and (3.12) from one side, and Eqs. (3.10), (3.13) and (3.14) from the other side form two different groups that suggest the different ranges of the Reynolds numbers  $Re_\omega$  for transitional flow, which is in line with the data from Table 3.2.

Equation (3.12) does not follow the original experiments [27, 28]. Corrected coefficient  $K_1 = 1.2 \times 10^{-13}$  (with the end of transition to turbulent flow at  $Re_\omega = 3.7 \times 10^5$ ) [1] is consistent with experiments [6, 27, 28] and Eq. (3.11) (Fig. 3.3). Equation (3.10) is in disagreement with Eqs. (3.12) and (3.13) for  $Re_\omega = (2.5\text{--}2.9) \times 10^5$  (Fig. 3.3).

Equation (3.13) conforms to the experiments [16], though its validity should be modified to the range  $Re_\omega = (1.9\text{--}2.75) \times 10^5$  [1]. Equation (3.14) deduced for large Schmidt numbers  $Sc = 1192\text{--}2465$  is in a good consistency with Eq. (3.13) for  $Sc = 2.28$ .

Roughness of the disk surface may provoke earlier transition to turbulent flow in comparison with a smooth disk. In laminar flow, surface roughness does not influence heat transfer. In experiments for  $Re_\omega > 5.6 \times 10^4$  [19, 69, 70], heat transfer increased very moderately at the expense of the enlarged surface area of a rough disk.

Surface roughness noticeably affects the boundaries of the flow regimes. The Reynolds number at onset of the spiral vortices (whose number diminished from 32 to 25) decreased from  $Re_\omega = 0.95 \times 10^5$  on a smooth disk to  $Re_\omega = 0.5 \times 10^5$  on a rough disk [58].

In experiments [57] on a rough disk, the onset of transition to turbulence began at  $Re_\omega = (0.23\text{--}1.23) \times 10^5$  (on a smooth disk, at  $Re_\omega = (2.4\text{--}2.63) \times 10^5$ ). The boundary of the end of transition also shifted down to  $Re_\omega = 2.55 \times 10^5$  on a rough disk in comparison with  $Re_\omega = 3.4 \times 10^5$  on the smooth disk in [58]. In the paper [18], the end of transition shifted down to  $Re_\omega = 2.0 \times 10^5$  on a rough disk as compared to  $Re_\omega = 2.7 \times 10^5$  on a smooth disk.

At the beginning of the transition to turbulent flow, the heat and mass transfer rate in the experiments [18] on a rough disk was by 34 % higher in comparison with a smooth disk over the range of the Reynolds numbers studied in that work.

### 3.3 Turbulent Flow

#### 3.3.1 Parameters of the Boundary Layer

Tangential  $v_\varphi$  and radial  $v_r$  velocity components described by the power-law function (2.40) and the quadratic Eq. (2.58), respectively, are in a good agreement with the experiments [7, 12] (see Figs. 2.2, 2.3 and 2.4). In addition, Eq. (2.58) conforms to the experimental data in the outer part of the boundary layer better than Eq. (2.41) (Fig. 2.4).

Temperature profiles  $\theta$  approximated by the power-law Eq. (2.53) at  $n_T = 1/4\text{--}1/5$  match well to the profiles measured in the work [6] for  $q_w = \text{const}$ . (see Fig. 2.5).

This chapter represents a validation of the present integral method (described in Chap. 2) in comparison with the von Karman's method, Eq. (2.41), often incorporated in many integral methods. On the basis of Eqs. (2.40) and (2.41) [71], the rest of boundary layer parameters can be written as Eqs. (2.77)–(2.81) with their constants expressed as [3, 4]

$$\alpha^2 = \frac{4(2 + 3/n)(1 + 2/n)(3 + 1/n)}{(16n^{-3} + 85n^{-2} + 145n^{-1} + 66)/n^2}, \quad (3.15)$$

$$\gamma^{(3n+1)/(n+1)} = C_n^{-2/(n+1)} \frac{2(n+1)(2n+2)(3n+1)(n+2)(1+\alpha^2)^{(1-n)/[2(n+1)]}}{3(11n+5)xn}, \quad (3.16)$$

$$\varepsilon_m = \frac{2\pi\alpha\gamma}{(1+n)(2+n)}, \quad \varepsilon_M = \frac{6\pi\alpha\gamma/n^2}{(1+1/n)(2+1/n)(1+2/n)}. \quad (3.17)$$

Constants  $\alpha$ ,  $\gamma$ ,  $\varepsilon_m$  and  $\varepsilon_M$  computed by Eqs. (2.83)–(2.86) (present integral method) and (3.15)–(3.17) (von Karman’s method) are listed in Table 3.4. Computed values for  $\gamma$ , and  $\varepsilon_M$  are practically identical for both methods at the same values of  $n$ , while the constants  $\alpha$  and  $\varepsilon_m$  representing the approximation of  $v_r$  are noticeably different.

Values of the flow swirl angle  $\alpha = \tan\varphi_w$  from Table 3.4 are plotted in Fig. 3.4 together with experiments [6, 7] and predictions by other models [72, 76]. Experimental data for the parameter  $\alpha$  behave as a decreasing function of the Reynolds number  $Re_\omega$  within the limits suggested by Eq. (2.83) at  $n = 1/7$  (upper) and  $n = 1/9$  (lower). The exponent  $n$  diminishes for larger  $Re_\omega$  [2, 3], which is followed with a decrease in the  $\alpha$  values (like in the experiments). The highest magnitude of  $\alpha = 0.162$  (at  $n = 1/7$ ) by von Karman’s Eq. (3.15) matches to the lowest level of  $\alpha$  found experimentally [6, 7, 72].

**Table 3.4** Constants of the solution for a free disk [1]

Coefficient	Equation, source	$n = 1/7$	$n = 1/8$	$n = 1/9$	$n = 1/10$
$C_n$	(2.49), [71]	8.74	9.71	10.6	11.5
$\alpha$	(2.83), [73]	0.2087	0.1842	0.1649	0.1493
$\alpha$	(3.15), [3]	0.162	0.143	0.128	0.116
$\gamma$	(2.84), [73]	0.5299	0.4977	0.4773	0.4597
$\gamma$	(3.16), [3]	0.526	0.497	0.479	0.463
$\varepsilon_m$	(2.85), [73]	0.1806	0.1542	0.1355	0.1204
$\varepsilon_m$	(3.17), [3]	0.219	0.187	0.164	0.146
$\varepsilon_M$	(2.86), [73]	0.1466	0.1127	0.0901	0.0734
$\varepsilon_M$	(3.17), [3]	0.1458	0.1122	0.0896	0.073

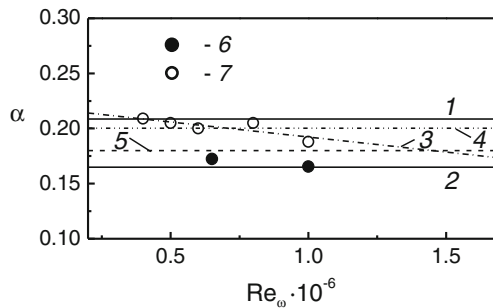


**Fig. 3.4** Tangent  $\alpha$  of the flow swirl angle at the wall [1]. Present integral method [1, 74, 75], Eq. (3.15): 1— $n = 1/7$ ; 2— $1/9$  (or  $1/7$ , von Karman [71]). 3—model [72]; 4—Eq. (2.44) [76],  $\alpha = 0.2003$  for  $n = 1/7$ ,  $b = 0.7$ ,  $c = 1.2$ ; 5—model [77]. Experiments: 6—[7]; 7—[6]

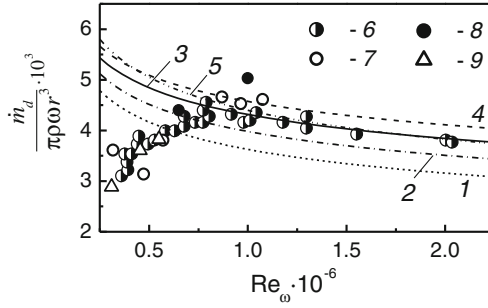


**Fig. 3.5** Dimensionless mass flow rate through the boundary layer [1]. Equation (2.85): 1— $n = 1/7$ ; 2— $1/8$ ; 3— $1/9$ ; 4— $1/10$ ; 5— $1/7$ , von Karman’s method (3.17) [71]. Experiments: 6—[72]; 7—[78]; 8—Shevchuk based on experimental data of [6]; 9—[79]

As it can be seen from Fig. 3.5, for  $Re_\omega \geq 0.75 \times 10^6$ , the dimensionless mass flow rate predicted by Eq. (2.85) for  $n = 1/9$  (the present integral method) is in good agreement with experiments [6, 72, 78] and predictions by the von Karman’s method for  $n = 1/7$ . For  $n = 1/7-1/8$  and  $Re_\omega = (0.5-0.75) \times 10^6$ , Eq. (2.85) also reasonably estimates the mass flow rate, although it incorrectly predicts the functional dependence of  $\dot{m}_d/(\rho_\infty \omega r^3)$  on  $Re_\omega$ . At the same time, approach [71] yields inaccurate predictions for  $Re_\omega = (0.5-0.75) \times 10^6$ .

Equation (2.42) for  $\alpha = 0.18$  for  $n = 1/7$  was employed in [77]. The value  $\alpha = 0.18$  insignificantly differs from the values by the present integral method given in Table 3.4.

In the work [79], velocity profiles did not exhibit self-similarity in turbulent flow over the range  $Re_\omega \approx (3.1-6.64) \times 10^5$ , whereas the wall value  $\alpha$  increased together with  $Re_\omega$  (or  $r/b$ ). The rather complicated integral method based on Eq. (2.43) and original experiments [79] tried to model this phenomenon. However, because of its excessive complexity, the method [79] was not developed further to include a model for heat transfer.

The work [72] also employed Eq. (2.42) together with an empirical equation for the mass flow rate in the boundary layer. However, the accuracy of this integral method did not exceed that of the von Karman’s method [71].

To conclude, the present integral method, Chap. 2, enables a more accurate prediction of the radial velocity distributions, values of  $\alpha$  and mass flow rate in the boundary layer than other integral methods. The values of the parameter  $n$  must be selected based on Figs. 2.2, 2.3, 2.4, 3.5 and 3.6, as well as the data for the Nusselt number presented below.

Predictions of the moment coefficient  $C_M$  by Eq. (2.80) for  $n = 1/7$  are in good agreement with the experiments in Fig. 3.2 for  $Re_\varphi < 2.0 \times 10^6$ . For larger values of  $Re_\varphi$ , predictions by Eq. (2.80) lie below the experiments. Values  $n = 1/8-1/10$  used in Eq. (2.80) shift the predictions close to experiments at  $Re_\varphi \geq 3.0 \times 10^6$  (see Fig. 3.2).

Logarithmic velocity profiles yield in the end the following equations for  $C_M$

$$C_M^{-1/2} = 1.97 \lg(Re_\varphi \sqrt{C_M}) + 0.03, \quad (3.18)$$

$$C_M = 0.982 (\lg Re_\varphi)^{-2.58}. \quad (3.19)$$

Equation (3.19) of Dorfman [2] yields the best overall match with the experiments, while Eq. (3.18) [80] sets the upper level restriction for the experimental data in Fig. 3.2.

In the paper [14] also employing a logarithmic model, the following approximation for the coefficient  $C_M$  was derived, which is valid over the range  $Re_\varphi \approx 4.0 \times 10^5 - 2.0 \times 10^6$

$$C_M = 0.13 Re_\varphi^{-0.185}. \quad (3.20)$$

Equation (3.20) agrees well with the experiments [12, 13] re-evaluated in [14], though it is by 5–10 % higher than the data of other authors for  $Re_\varphi \geq 2.0 \times 10^6$  (see Fig. 3.2).

Logarithmic velocity profiles entail noticeable complications of mathematical models; therefore they were practically rarely used in integral methods.

### 3.3.2 Surface Heat Transfer: Different Experiments and Solutions

The integral method of Dorfman [2], applied together with the boundary condition (2.30) and  $n_R = 0.8$ , yielded known solutions for the coefficients  $K_1$  and  $K_2$  in Eq. (3.4)

$$K_1 = 0.0197(n_* + 2.6)^{0.2} Pr^{0.6}, \quad (3.21)$$

$$K_2 = K_1(n_* + 2)/(n_* + 2.6). \quad (3.22)$$

The multiplier  $Pr^{0.6}$  was obtained by the authors [3, 4].

Table 3.5 represents results for the coefficients  $K_1$  and  $K_2$  depending on  $n_*$  and computed by Eqs. (3.21) and (3.22) together with experimental data from different sources. Measurements [17, 61, 81–83] for  $T_w = \text{const.}$  (or  $n_* = 0$ ) made mainly in 1950th and 1960th are in good agreement with Eqs. (3.21) and (3.22). However, the modern accurate measurements for  $K_1$  are lower than the Dorfman's predictions in Table 3.5: by 4.4 % [6, 15, 23, 62, 63] and 9.5 % [84]. Experimental values [62, 63] are estimations made by the author of the present work based on the published data.

For the thermal boundary condition  $q_w = \text{const.}$  (or  $n_* = -0.6$ ), the coefficient  $K_1$  in measurements [6, 27, 28] was by 14.1 % smaller than the estimation by

**Table 3.5** Values of the constants  $K_1$  and  $K_2$  for  $n_R = 0.8$  and  $Pr = 0.72$  [1]

Coefficient	Source or equation	$n_* = -0.6$	$n_* = 0$	$n_* = 2$	$n_* = 6$
$K_2$	[17, 61, 81, 82]		0.015		
$K_1$	[83]		0.0194		
$K_1$	[84]		0.0179		
$K_2$	[84]		0.0138		
$K_1$	[6, 15, 23, 62, 63]		0.0188		
$K_2$	[23, 62]		0.0145		
$K_1$	[6, 27, 28]	0.0163			
$K_1$	Dorfman, Eq. (3.21)	0.0186	0.0196	0.022	0.0249
$K_2$	Dorfman, Eq. (3.22)	0.013	0.0151	0.0191	0.0231

Eq. (3.21) (Table 3.5). CFD simulations [85] for  $q_w = \text{const.}$  are approximated by Eq. (3.4) at  $n_R = 0.83$  and  $K_1 = 0.0111$ ,  $K_2 = 0.0086$ . Authors [81] obtained the same value  $K_2 = 0.015$  for the cases  $q_w = \text{const.}$  and  $T_w = \text{const.}$ , which does not look trustworthy.

For  $n_* = -0.2$ , predictions by Eqs. (3.21) and (3.22) by up to 10 % surpass the Nusselt numbers measured in [86, 87]. Empirical values of the coefficient  $K_1$  were not estimated in [86, 87], apparently because the  $T_w$  distribution did not comply with Eq. (2.30).

The so called theory of local modelling [2–4, 88] (see Sect. 2.3.2) yields a solution for the Nusselt number for the situation, where Eq. (2.30) does not hold. This solution proved to be insufficiently accurate and has therefore not been further developed.

**Average Nusselt number for an entire disk.** Average Nusselt numbers  $Nu_{\text{av}}$  for an entire disk, where laminar, transitional and turbulent flows co-exist simultaneously, are often of interest in technical applications.

It was assumed in the model [61] that transition to turbulence takes place abruptly at the Reynolds number  $Re_{\omega, \text{tr}}$  calculated at a coordinate  $r_{\text{tr}}$ . Following this assumption, one can present  $Nu_{\text{av}}$  (see its definition in Nomenclature) as follows

$$Nu_{\text{av}} = \frac{b \left[ \int_0^{r_{\text{tr}}} Nu_{\text{lam}} (T_w - T_\infty) dr + \int_{r_{\text{tr}}}^b Nu_{\text{turb}} (T_w - T_\infty) dr \right]}{\int_{r_{\text{tr}}}^b (T_w - T_\infty) r dr}. \quad (3.23)$$

The Nusselt numbers to be substituted in Eq. (3.23) are defined by Eq. (3.4) for  $Nu$ , where the constants are  $K_{1, \text{lam}}$ ,  $n_R = 1/2$  for laminar flow, and  $K_{1, \text{turb}}$ ,  $n_R$  for turbulent flow.

If the disk temperature is described by Eq. (2.30), this yields [1]

$$Nu_{\text{av}} = K_{1, \text{lam}} Re_{\omega, \text{tr}}^{1/2} \left( \frac{Re_{\omega, \text{tr}}}{Re_\varphi} \right)^{n_*/2+1/2} + \frac{2+n_*}{2n_R+1+n_*} K_{1, \text{turb}} Re_\varphi^{n_R} \left[ 1 - \left( \frac{Re_{\omega, \text{tr}}}{Re_\varphi} \right)^{n_*/2+n_R+1/2} \right]. \quad (3.24)$$

For  $T_w = \text{const.}$  (or  $n_* = 0$ ), Eq. (3.24) simplifies to [1]

$$Nu_{av} = K_{1,\text{lam}} Re_{\omega,\text{tr}}^{1/2} \left( \frac{Re_{\omega,\text{tr}}}{Re_\varphi} \right)^{1/2} + \frac{2}{2n_R + 1} K_{1,\text{turb}} Re_\varphi^{n_R} \left[ 1 - \left( \frac{Re_{\omega,\text{tr}}}{Re_\varphi} \right)^{n_R+1/2} \right]. \quad (3.25)$$

Equation (3.24) holds, if  $Re_\varphi \geq Re_{\omega,\text{tr}}$ . Given  $Re_\varphi < Re_{\omega,\text{tr}}$ , the second term in Eq. (3.24) vanishes. Asymptotically at  $Re_\varphi \gg Re_{\omega,\text{tr}}$ , the turbulent flow fully occupies a disk, and Eq. (3.24) turns into Eq. (3.4) for  $Nu_{av}$ , where [1]

$$K_{2,\text{turb}} = \frac{2 + n_*}{2n_R + 1 + n_*} K_{1,\text{turb}}. \quad (3.26)$$

Once  $n_R = 0.8$ , Eqs. (3.22) and (3.26) become identical.

In Fig. 3.6, curve 4 is based on Eq. (3.25) for the case  $T_w = \text{const.}$  and the values  $n_R = 0.8$ ,  $2K_{1,\text{turb}}/(2n_R + 1) = 0.015$ ,  $K_{1,\text{lam}} = 0.4$ ,  $Re_{\omega,\text{tr}} = 2.4 \times 10^5$  [61]. Curve 4 lies by 15 % lower than the original experimental data [61] for  $Re_\omega \leq 6.5 \times 10^5$ . A smaller value of  $Re_{\omega,\text{tr}} = 2.0 \times 10^5$  (curve 5) provides a better match of Eq. (3.25) with experiments [1].

### 3.3.3 Effect of Approximation of the Radial Velocity Profile

Effect of the tangent of the flow swirl angle was taken into account via a model

$$\tan\varphi = \alpha(1 - \xi)^\sigma. \quad (3.27)$$

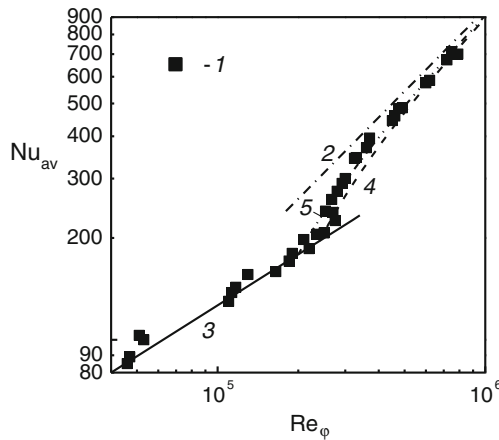


**Fig. 3.6** Average Nusselt numbers of an *entire* disk rotating in still air [1]. Experiments: 1—[61]. Calculations by Eq. (8.4): 2—developed turbulent flow,  $n_R = 0.8$ ,  $K_2 = 0.015$  (Table 3.5) [61]; 3—laminar flow,  $n_R = 1/2$ ,  $K_1 = 0.4$  [61]. Calculation of  $Nu_{av}$  for an *entire* disk: 4—Eq. (3.25) at  $Re_{\omega,\text{tr}} = 2.4 \times 10^5$  [61]; 5—Eq. (3.25) at  $Re_{\omega,\text{tr}} = 2.0 \times 10^5$  [1]

For the constant  $\sigma$ , the values  $\sigma = 2, 1$  and  $0$  were selected, which enabled undertaking parametric studies, whereas the value  $\sigma = 2$  remained the major one in the present integral method. In the end, solutions for the parameters in Eqs. (2.77)–(2.87) look as

$$\alpha = \left[ \frac{C_1}{(3 + m)B_0 + (4 + m)D_0} \right]^{1/2}, \tag{3.28}$$

$$H_9 = \alpha D_0(4 + m), \tag{3.29}$$

$$\varepsilon_M = 8\pi\alpha\gamma D_0. \tag{3.30}$$

Here  $B_0 = B_1$  and  $D_0 = D_1$  for  $\sigma = 2$ ;  $D_0 = 1/(n + 1) - 1/(n + 2) - 1/(2n + 1) + 1/(2n + 2)$  and  $B_0 = D_2$  for  $\sigma = 1$ ;  $B_0 = 1/(2n + 1)$  and  $D_0 = 1/(n + 1) - 1/(2n + 1)$  for  $\sigma = 0$  [1]. The case with  $\sigma = 2$  coincides with Eqs. (2.83)–(2.87) at  $\kappa = 0, \beta = 0$ .

The effect of the exponent  $\sigma$  on the radial velocity profiles is elucidated in Fig. 3.7.

Table 3.6 lists numerical data for the constants  $\alpha, \gamma$  and  $\varepsilon_M$  computed by Eqs. (3.28)–(3.30) (data for  $\sigma = 1$  and  $2$  partially repeat those from Table 3.4).

In Fig. 3.7, the radial velocity profile for  $\sigma = 0$  is qualitatively and quantitatively different from the other  $v_r$  profiles. Anyway, in spite of this, the deviation of the calculated  $C_M$  values for  $\sigma = 0$  from the basic case of  $\sigma = 2$  is 5 % at maximum (Table 3.6).

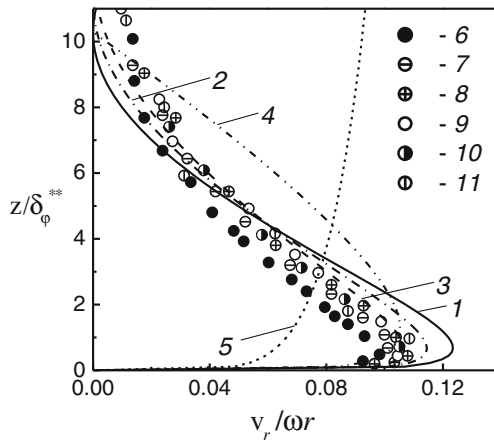


**Fig. 3.7** Profiles of the radial velocity component in the turbulent boundary layer over a free rotating disk [1]. 1— $n = 1/7$ , 2— $1/8$ , 3— $1/9$ . Equation (2.41), [71]: 4— $n = 1/7$ . Equation (2.44): 5— $\sigma = 0, n = 1/7$ . Experiments: 6— $Re_\omega = 0.4 \times 10^6$ , 7— $0.65 \times 10^6$ , 8— $0.94 \times 10^6$ , 9— $1.6 \times 10^6$  [12], 10— $0.6 \times 10^6$ , 11— $1.0 \times 10^6$  [7]

**Table 3.6** Constants in Eqs. (2.77)–(2.80), (3.28) and (3.30)–(3.41) at different  $\sigma$  [1, 89]

Coefficient	$n = 1/7$	$n = 1/8$	$n = 1/9$	$n = 1/10$
$\alpha, \sigma = 2$	0.2087	0.1842	0.1649	0.1493
$\alpha, \sigma = 1$	0.162	0.143	0.128	0.116
$\alpha, \sigma = 0$	0.0925	0.0818	0.0733	0.0664
$\gamma, \sigma = 2$	0.530	0.4977	0.4773	0.4597
$\gamma, \sigma = 1$	0.526	0.497	0.479	0.463
$\gamma, \sigma = 0$	0.616	0.588	0.571	0.556
$\varepsilon_M, \sigma = 2$	0.1466	0.1127	0.0901	0.0734
$\varepsilon_M, \sigma = 1$	0.146	0.112	0.09	0.073
$\varepsilon_M, \sigma = 0$	0.139	0.107	0.086	0.0704
$K_V, \sigma = 2$	0.203	0.183	0.1661	0.1523
$K_V, \sigma = 1$	0.167	0.15	0.1364	0.125
$K_V, \sigma = 0$	0.111	0.10	0.0909	0.0833
$K_3, \sigma = 2$	0.02683	0.02079	0.01673	0.0137
$K_3, \sigma = 1$	0.0267	0.0207	0.0166	0.0136
$K_3, \sigma = 0$	0.0255	0.0198	0.016	0.0131
$n_R$	0.8	0.8182	0.8333	0.8462
$m$	0.6	0.6363	0.6667	0.6923
$n_p, \sigma = 2$	0.5018	0.4894	0.4797	0.4719
$n_p, \sigma = 1$	0.48	0.471	0.463	0.457
$n_p, \sigma = 0$	0.45	0.444	0.44	0.436

Equation (2.70), complemented with Eqs. (3.27)–(3.30), can be analytically solved only for the condition  $\Delta \geq 1$  [75, 89]. For  $\sigma = 2$ , such a solution degenerates to Eqs. (2.89)–(2.91) at  $N = 0$  and  $\beta = 0$ .

Thus, for  $\Delta \geq 1$ , the coefficients in Eq. (3.4) can be written as

$$n_R = (n + 1)/(3n + 1), \quad (3.31)$$

$$K_1 = K_3 \Delta^{-n} Pr^{1-n_p}, \quad (3.32)$$

$$\Delta^{-n} = \left[ \frac{4 + m}{2 + m + n_*} K_V Pr^{-n_p} + (1 - K_V) \right]^{-1}, \quad (3.33)$$

$$K_1 = K_3 Pr \left[ \frac{4 + m}{2 + m + n_*} K_V + (1 - K_V) Pr^{n_p} \right]^{-1}, \quad (3.34)$$

$$K_2 = K_1 (n_* + 2)/(2 + n_* + m), \quad (3.35)$$

$$K_3 = A_c (1 + \alpha^2)^{1/2} = C_n^{-2/(n+1)} \gamma^{-2n/(n+1)} (1 + \alpha^2)^{0.5(1-n)/(n+1)}, \quad (3.36)$$

$$K_V = 1 - D_{2^*}/A_{1^*}. \quad (3.37)$$

In Eq. (3.37), the constants are defined as [1]:  $D_{2^*} = D_2$  and  $A_{1^*} = A_1$  for  $\sigma = 2$ ;  $D_{2^*} = 1/(2n + 1) - 1/(2n + 2)$  and  $A_{1^*} = 1/(n + 1) - 1/(n + 2)$  for  $\sigma = 1$ ;  $D_{2^*} = 1/(2n + 1)$  and  $A_{1^*} = 1/(n + 1)$  for  $\sigma = 0$ . Parameters  $K_3$  and  $K_V$  presented in Table 3.6 do not depend on  $n_*$ . In view of the relation  $2n_R = 1 + m$  [which follows from Eqs. (2.78) and (3.31)], Eqs. (3.35) and (3.26) become identical.

Let us denote  $G = Pr^{n_p}(2 + m + n_*)/(4 + m)$ , use the Taylor's series expansion of the entire term in brackets in Eq. (3.34) for  $Pr \rightarrow 1$ ,  $n_* \rightarrow 2$  in the neighborhood of  $G = 1$  and neglect summands of an infinitesimal order. As a result, one can obtain [74, 75, 89]

$$Nu = K_3 \left( \frac{2 + m + n_*}{4 + m} \right)^{K_V} Re_{\omega}^{n_R} Pr^{1 - n_p(1 - K_V)}. \quad (3.38)$$

Let us further consider a solution for the most widely used value  $n = 1/7$  and round down:  $K_V = 0.2$ . In doing so, Eq. (3.38) becomes identical to the Dorfman's solution (3.21), if one sets the overall exponent for the  $Pr$  number equal to 0.6 and keeps this unchanged and independent of  $n$ . Based on this, the unknown parameter  $n_p$  can be determined as

$$n_p = 0.4/(1 - K_V). \quad (3.39)$$

Table 3.6 contains numerical values of the parameter  $n_p$  calculated by Eq. (3.39). Equation (3.38) coincides with Eq. (3.34) solely for  $Pr \rightarrow 1$  and  $n_* \rightarrow 2$ . A mathematical interpretation of this fact is that Eq. (3.38) represents a particular case of Eq. (3.34).

For  $\Delta \leq 1$  and  $N = 0$  and  $\beta = 0$  (a single rotating disk), Eq. (2.89) remains transcendental

$$\Delta^{2n+1} (a_* - 2b_*\Delta + c_*\Delta^2) = \frac{4 + m}{2 + m + n_*} (a_* - 2b_* + c_*) Pr^{-n_p}. \quad (3.40)$$

In Eq. (3.40),  $n_T = n$  has been set and the subscript "T" at the coefficients  $a_*$ ,  $b_*$  and  $c_*$  has been omitted. Equation (3.40) holds for the case  $Pr \geq 1$  (or  $Sc \geq 1$ ): naphthalene sublimation in air, flows of liquids etc. Therefore, an analysis of Eq. (3.40) is relegated to Chap. 6.

Table 3.7 and Fig. 3.8 illustrate the influence of the parameter  $\sigma$  on the coefficients  $K_1$  and  $K_2$  in Eqs. (3.34) and (3.35) [as compared to Eqs. (3.21) and (3.22)] in a form of a dependence on the parameter  $n_*$  for  $Pr$  numbers 0.72 (air) and 1.0. Equation (3.34) at  $\sigma = 2$  demonstrates the best agreement with experiments, especially for  $n_* \leq 0$ , which **confirms the choice of the value  $\sigma = 2$  as a major one in the present integral method.**

**Table 3.7** Constants in Eqs. (3.34) and (3.35) for different values  $\sigma$  [75, 89]

Coefficient	Equation	$n_* = -0.6$	$n_* = 0$	$n_* = 2$	$n_* = 6$
Calculation for $Pr = 0.72$					
$K_1$	Equation (3.34), $\sigma = 2$	0.0169	0.0187	0.022	0.0246
$K_2$	Equation (3.35), $\sigma = 2$	0.0118	0.0144	0.0191	0.0229
$K_1$	Equation (3.34), $\sigma = 1$	0.0176	0.0191	0.0219	0.0240
$K_1$	Equation (3.34), $\sigma = 0$	0.0180	0.0191	0.0209	0.0222
Calculation for $Pr = 1$					
$K_1$	Dorfman, Eq. (3.21)	0.0226	0.0238	0.0267	0.0303
$K_2$	Dorfman, Eq. (3.22)	0.0158	0.0183	0.0232	0.0282
$K_1$	Equation (3.34), $\sigma = 2$	0.0212	0.0232	0.0268	0.0296
$K_2$	Equation (3.35), $\sigma = 2$	0.0149	0.0178	0.0233	0.02755
$K_1$	Equation (3.34), $\sigma = 1$	0.0219	0.0237	0.0267	0.0289
$K_1$	Equation (3.34), $\sigma = 0$	0.0222	0.0235	0.0255	0.0269

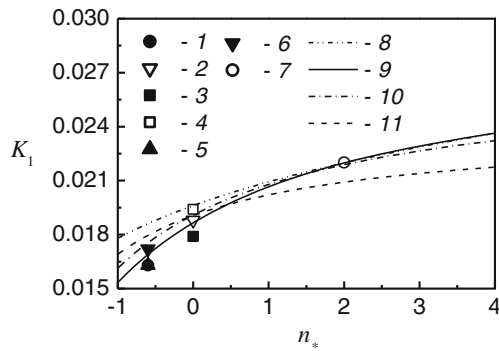


**Fig. 3.8** Effect of the exponents  $n_*$  and  $\sigma$  on the constant  $K_1$  in turbulent air flow ( $Pr = 0.72$ ) [1]. Experiments: 1—[6, 27, 28]; 2—[15, 23, 62, 63]; 3—[84]; 4—[83]; 5—[85],  $K_1$ , lower limit; 6—[85],  $K_1$ , upper limit; 7—[2, 3, 4]. Calculations: 8—Eq. (3.21) [2]; 9—Eq. (3.34),  $\sigma = 2$ ; 10—Eq. (3.34),  $\sigma = 1$ ; 11—Eq. (3.34),  $\sigma = 0$

Data in Tables 3.5 and 3.7 elucidate also inaccuracies of the Dorfman’s Eqs. (3.21) and (3.22), which amplify as soon as the Prandtl number diverges from unity.

Figure 3.3 demonstrates that the local Nusselt numbers by Eq. (3.34) at  $K_1 = 0.0169$  for  $q_w = \text{const.}$  and  $K_1 = 0.0187$  for  $T_w = \text{const.}$  agree well with experiments [6].

Using the definition of the  $Nu$  number and Eq. (3.4), one can determine the exponent  $n_*$  in Eq. (2.30) for the boundary condition  $q_w = \text{const.}$  [26]

$$\frac{T_w - T_\infty}{T_\infty} = \frac{q_w b}{\lambda T_\infty K_1} Re_\varphi^{-(n+1)/(3n+1)} x^{(n-1)/(3n+1)}. \quad (3.41)$$

For the case  $q_w = \text{const.}$ , Eq. (3.41) yields the value  $n_* = (n - 1)/(3n + 1) = -m$  [26]. Table 3.6 summarizes the values of the parameter  $m$  calculated at different values of  $n$ .

Experimental disk temperature distributions measured in [6] are depicted in Fig. 3.9. Flow was turbulent at  $Re_\omega > 3.6 \times 10^5$  [6]. For  $Re_\varphi = 1.6 \times 10^6$  illustrated in Fig. 3.9, the turbulent region was localized over the span  $x = 0.474\text{--}1.0$ . The disk itself comprised three annular regions [6]: an unheated region at  $x = 0\text{--}0.15$ ; regions  $x = 0.15\text{--}0.4$  and  $0.4\text{--}0.96$  heated via two separate heaters having the same power. Data 1 and 2 correspond to the cases with both heaters or only the external one switched on, respectively.

For the case 1, calculations have only been performed for the region  $x > 0.5$ , where the disk temperature predicted by Eq. (3.41) at  $q_w = \text{const.}$  (i.e.  $n_* = -0.6$ ) fairly well matches the measurements. Here the experimental data are:  $K_1 = 0.0163$ ,  $q_w = 710 \text{ W/m}^3$ ,  $T_\infty = 298.9 \text{ K}$ ,  $Re_\varphi = 1.6 \times 10^6$ ,  $b = 0.5 \text{ m}$ ;  $\lambda = 0.02624 \text{ W/(m K)}$  for air at  $T_\infty \approx 300 \text{ K}$  [90].

The wall temperature distribution in the heated region  $x > 0.5$  in case 2 (internal heater off) was practically constant (see Fig. 3.9).

Thus, for the case  $q_w = \text{const.}$  (or  $n_* = -0.6$ ), the constant  $K_1 = 0.0169$  calculated by Eq. (3.34) at  $n = 1/7$ ,  $n_R = 0.8$  and  $\sigma = 2$  differs from the measured value  $K_1 = 0.0163$  [6, 27, 28] by only 3.7 %. Dorfman's constant  $K_1 = 0.0186$  by Eq. (3.21) diverts from the measurements by 14.1 %. For  $1/n = 8.7647$  and  $n_R = 0.83$ , Eq. (3.34) yields the value  $K_1 = 0.0115$ , which means only 3.6 % mismatch to the value  $K_1 = 0.0111$  obtained in simulations [85].

For the case  $T_w = \text{const.}$  (or  $n_* = 0$ ), the value  $K_1 = 0.0187$  ( $T_w = \text{const.}$ ) calculated by Eq. (3.4) at  $n = 1/7$ ,  $n_R = 0.8$  and  $\sigma = 2$  much better than  $K_1 = 0.0196$  by Dorfman's formula (3.21) agrees with experimental value  $K_1 = 0.0188$  [6, 15, 23, 62, 63] (deviation 0.5 %).

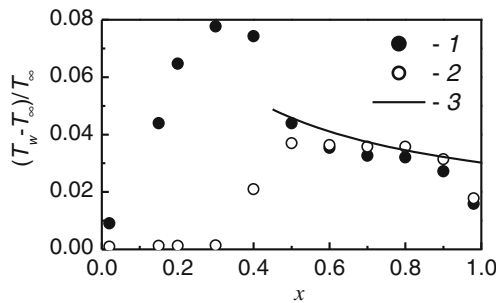


**Fig. 3.9** Experimental temperature distribution [6] and its computation over the surface of a rotating disk [1]. 1— $q_w = \text{const.}$ ; 2— $T_w \approx \text{const.}$  Computation [26]: 3—Eq. (3.41)

### 3.3.4 Arbitrary Distribution of the Wall Temperature

The disk temperature distributions  $T_w$  measured in experiments [86, 87], Fig. 3.10, do not agree with the analytical approximations by Eqs. (2.29) and (2.30). Reliability of these experimental data was proved in [50] by a numerical solution of the differential Eqs. (2.9)–(2.15) using the Cebeci–Smith model of turbulence [90]. A numerical version of Dorfman’s method ( $n = 1/7$ ) was employed in [86, 87] to model these experimental conditions. Numerically computed Nusselt numbers, similarly to those obtained by the analytical Dorfman’s method, agreed well with the experiments for  $dT_w/dr > 0$  and noticeably exceeded them for  $dT_w/dr \approx 0$  and  $dT_w/dr < 0$  [86, 87].

The numerical version of the present integral method, Eqs. (2.72) and (2.73), was used by the author [91] to simulate the experimental conditions [86, 87].

Experimental disk temperature distributions were divided in [86, 87] into four groups complying with Eq. (2.30) at positive ( $n_* = 0.4$  and  $0.6$ ), approximately constant ( $n_* = 0.1$ ), and negative ( $n_* = -0.2$ ) gradients of the wall temperature  $T_w$ . Scatter of the distributions of  $T_w$  within each group was less than 10–15 % for different values of  $Re_\varphi$ .

Agreement of Eq. (2.30) with the measurements at the  $n_*$  values mentioned above is rather conventional. Obviously, Eq. (2.30) does not assume maxima, minima and inflection points visible in curves depicted in Fig. 3.10 within the region of determination of  $T_w$ . However, for convenience, this classification was left unchanged here.

Computed local Nusselt numbers are depicted in Figs. 3.11, 3.12 and 3.13. Experimental distributions of  $T_w$  used as the boundary conditions were

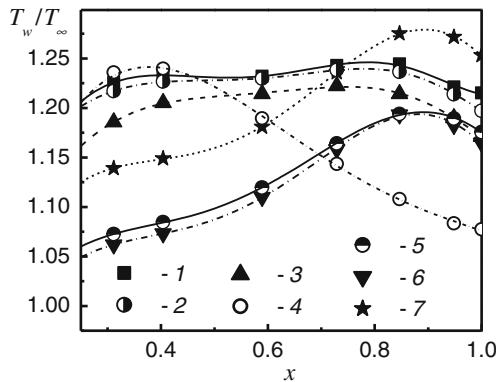


**Fig. 3.10** Disk temperature variation: symbols—experiments [87], lines—polynomial approximations of the experiments by [1]. 1— $n_* = 0.1$ ,  $Re_\varphi = 1.135 \times 10^6$ ; 2— $n_* = 0.1$  and  $Re_\varphi = 1.19 \times 10^6$ ; 3— $n_* = 0.1$  and  $Re_\varphi = 3.2 \times 10^6$ ; 4— $n_* = -0.2$  and  $Re_\varphi = 2.65 \times 10^6$ ; 5— $n_* = 0.4$  and  $Re_\varphi = 2.67 \times 10^6$ ; 6— $n_* = 0.4$  and  $Re_\varphi = 3.14 \times 10^6$ ; 7— $n_* = 0.6$  and  $Re_\varphi = 1.59 \times 10^6$ ;  $x = r/b$

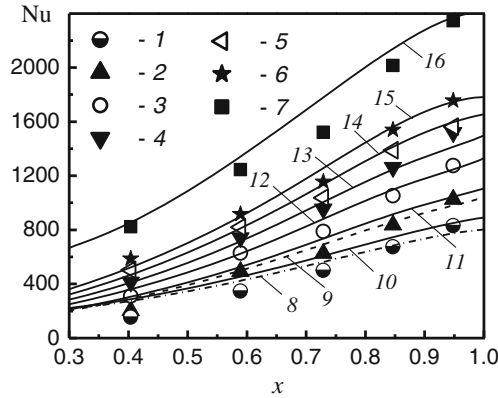


**Fig. 3.11** Variation of the Nusselt number for  $n_* = 0.1$ : symbols 1–7—experiments [87]. Lines—simulations [1, 91]: 8— $n = n_T = 1/5$ ; 9— $n = 1/6, n_T = 1/5$ ; 10–16— $n = n_T = 1/6$ . 1, 8, 10— $Re_\phi = 0.819 \times 10^6$ ; 2, 9, 11— $Re_\phi = 1.08 \times 10^6$ ; 3, 12— $Re_\phi = 1.35 \times 10^6$ ; 4, 13— $Re_\phi = 1.6 \times 10^6$ ; 5, 14— $Re_\phi = 1.88 \times 10^6$ ; 6, 15— $Re_\phi = 2.14 \times 10^6$ ; 7, 16— $Re_\phi = 3.2 \times 10^6$ ;  $x = r/b$

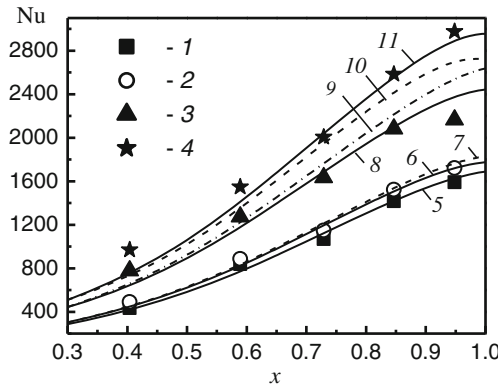


**Fig. 3.12** Radial variation of the Nusselt number [1]. Case  $n_* = 0.6$ : 1, 2—experiments [87]; 5, 6—calculations,  $n = n_T = 1/6.5$ ; 7—calculation,  $n = n_T = 1/7$ . Case  $n_* = 0.4$ : 3, 4—experiments [87]; 8, 10—calculations,  $n = n_T = 1/6$ ; 9, 11—calculations,  $n = n_T = 1/7$ . Reynolds numbers  $Re_\phi$ : 1, 5— $1.59 \times 10^6$ ; 2, 6, 7— $1.71 \times 10^6$ . 3, 8, 9— $2.67 \times 10^6$ ; 4, 10, 11— $3.14 \times 10^6$

approximated by a 7th-order polynomial, see Fig. 3.10 [1, 91]. Comparisons of the simulations with the experimental data enabled developing hints for the choice of the  $n$  and  $n_T$  values.

Results for the case  $n_* = 0.1$  are plotted in Fig. 3.11 [1, 91]. Computations and experiments for  $Re_\phi = 1.08 \times 10^6$ – $3.2 \times 10^6$  match well for  $n = n_T = 1/6$ , though values  $n = n_T = 1/5$  provide a better agreement for the smaller value  $Re_\phi = 0.819 \times 10^6$ .

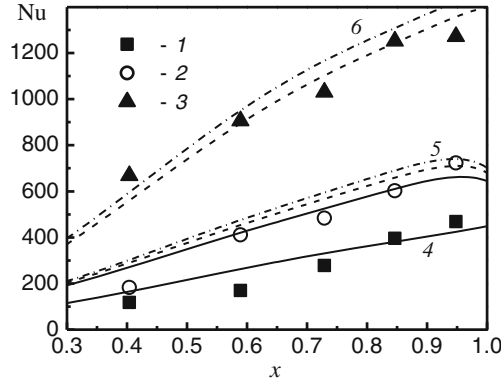


**Fig. 3.13** Radial variation of the Nusselt number [1]. Case  $n_* = -0.2$ : 1–3—experiments [87]. Calculations [91]: solid lines 4, 5— $n = 1/6$ ,  $n_T = 1/4$ ; dashed lines 5, 6— $1/6$  and  $1/5$ ; dash-dotted lines 5, 6—both  $1/6$ . Reynolds numbers  $Re_\varphi$ : 1, 4— $0.548 \times 10^6$ ; 2, 5— $1.08 \times 10^6$ ; 3, 6— $2.65 \times 10^6$

Figure 3.12 depicts calculations for similar cases  $n_* = 0.4$  and  $n_* = 0.6$  [1, 91]. At smaller Reynolds numbers  $Re_\varphi < 1.71 \times 10^6$ , a better agreement with experiments is yield using the exponents  $n = n_T = 1/6.5$ . For the larger values  $Re_\varphi = 2.67 \times 10^6$  and  $3.14 \times 10^6$ , exponents  $n = n_T = 1/6$  and  $1/7$ , respectively, are required. Exponents  $n$  and  $n_T$  for the simulations in Fig. 3.12 are slightly smaller as compared to the case  $n_* = 0.1$ , where  $dT_w/dr \approx 0$  (Fig. 3.11).

In Fig. 3.13, for the negative wall temperature gradient  $dT_w/dr < 0$  ( $n_* = -0.2$ ), the values of  $n_T = 1/4$  and  $n = 1/6$  were needed for  $Re_\varphi = (0.548-1.08) \times 10^6$ . Exponents  $n_T = 1/5$  and  $n = 1/6$  were used for a larger value  $Re_\varphi = 2.65 \times 10^6$ . Thus, for the same value of the Reynolds number  $Re_\varphi$ , the negative gradient  $dT_w/dr < 0$  entails the need to use a larger value  $n_T$ , whereas the value  $n = 1/6$  remains the same (in comparison with the data in Fig. 3.11).

Profiles of the velocity and temperature were not obtained in the measurements [86, 87]. Because of this, an estimation of the exponents  $n$  and  $n_T$  is made based on the distribution of the Nusselt number. The lower rate of the radial variation in the  $Nu$  numbers in Fig. 3.13 (case  $n_* = -0.2$ ) results in a smaller value of the exponent  $n_R$  in Eq. (3.4) and, hence, larger exponents  $n$  and  $n_T$ . Numerical simulations confirm this trend. The experimental investigation [6], among other results, revealed that temperature profiles for  $q_w = \text{const.}$  ( $dT_w/dr < 0$ ,  $n_* \approx -0.6$ ) and  $Re_\omega = 10^6$  were characterized by the exponents  $n_T = 1/4-1/5$  (see Fig. 2.5). These exponents correlate with our simulations for the case of  $n_* = -0.2$ .

To conclude, in case of an arbitrary variation of the disk temperature, predictions of turbulent heat transfer of a rotating disk using a numerical version of the present integral method match well with the experiments [87], whereas the exponent  $n_T$  in the temperature profile approximation depends on the thermal boundary conditions.

### 3.4 Generalized Analytical Solution for Laminar and Turbulent Flow

As said above, Dorfman's Eq. (3.6) for the Nusselt number in laminar regime at  $Pr = 1-0.1$  by up to 238 % exceeds the self-similar solution, Table 3.1. The more accurate Eqs. (3.7) and (3.8) [31, 32] are valid only for  $T_w = \text{const.}$  ( $n_* = 0$ ). To improve this situation, an approximate solution for the Nusselt number valid over the range  $Pr = 1-0.1$  and possessing significantly higher accuracy than Eq. (3.6) was derived in [1, 29, 30].

Equation (2.18) of the velocity boundary layer and Eq. (2.20) of the thermal boundary layer were rewritten as

$$\frac{d}{dr} [r^4 \delta K_V K_m] = \frac{c_f}{2} r^4 (1 + \alpha^2)^{1/2}, \quad (3.42)$$

$$\frac{d}{dr} [r^2 \delta K_H K_m (T_w - T_\infty)] = \chi \frac{c_f}{2} r^2 (1 + \alpha^2)^{1/2} (T_w - T_\infty). \quad (3.43)$$

Here  $\chi$  is the Reynolds analogy parameter defined by Eq. (2.52).

The parameters for the turbulent boundary layer are given by Eqs. (2.77)–(2.82); additional conditions are  $K_V = \text{const.}$  and  $K_m = \text{const.}$  The majority of the constants in Eqs. (2.77)–(2.82) for turbulent flow are listed in Sect. 2.5, while  $K_m = \alpha A_1$ ,  $K_V = 1 - D_2/A_1$ .

By setting  $n = 1$  and  $m = 0$ , Eqs. (2.77)–(2.82) can be used also for laminar flow. The constants in Eqs. (2.77)–(2.82) for laminar flow were first obtained in [3, 4] by solving and integrating the self-similar Eqs. (2.32)–(2.35)

$$a = 0.8284, \quad K_V = 0.3482, \quad K_m = \frac{I_\infty \alpha}{\delta(\omega/\nu)^{1/2}} = \frac{I_\infty \alpha}{\gamma}, \quad (3.44)$$

$$I_\infty = \alpha^{-1} \int_0^\infty \frac{v_r}{\omega r} d(z\sqrt{\omega/\nu}) = 0.5338, \quad A_c = 0.6159(1 + \alpha^2)^{-1/2}. \quad (3.45)$$

If boundary condition (2.30) holds, the dimensionless temperature  $\theta$  and shape-factor of the temperature profile  $K_H$  are also self-similar, i.e. independent of the coordinate  $r$ . Substituting Eqs. (2.30), (2.77)–(2.82), (3.44) and (3.45) into Eqs. (3.42) and (3.43) yields

$$(4 + m)\gamma K_V K_m = A_c(1 + \alpha^2)^{1/2}, \quad (3.46)$$

$$(2 + m + n_*)\gamma K_H K_m = \chi A_c(1 + \alpha^2)^{1/2}. \quad (3.47)$$

Equation (3.47) contains two unknown quantities:  $K_H$  and  $\chi$ , which can be connected by Eq. (2.51) of Dorfman [2]. The present integral method for turbulent

flow validated in Sect. 3.3 enables elaborating a novel model linking  $K_H$  and  $\chi$ , which is much more accurate than Eq. (2.51) and originates automatically from our boundary layer model [29]

$$b_2 K_H = 1 - \chi Pr^{n_p} (1 - K_V) b_1. \quad (3.48)$$

Correction multipliers  $b_1$  and  $b_2$  take account of laminar flow. These multipliers are equal to unity for turbulent flow, and the exponent  $n_p$  is defined by Eq. (3.39).

Solving Eq. (3.47) with account for Eq. (2.52), one can assure that the first of Eq. (3.4) again describes the Nusselt number at  $n_R = (n + 1)/(3n + 1)$  and

$$K_1 = (2 + m + n_*) \gamma K_H K_m Pr. \quad (3.49)$$

If one equates the relations for  $\chi$  resulting from Eqs. (3.47) and (3.48), derives  $K_H$  from this equation and substitutes it into Eq. (3.49), this yields

$$K_1 = A_c (1 + \alpha^2)^{1/2} Pr \left[ \frac{4 + m}{2 + m + n_*} K_V b_2 + (1 - K_V) Pr^{n_p} b_1 \right]^{-1}, \quad (3.50)$$

$$K_3 = A_c (1 + \alpha^2)^{1/2}. \quad (3.51)$$

Equations (3.50) and (3.34) coincide for turbulent flow, where  $b_1 = 1$  and  $b_2 = 1$ . Setting  $n = 1$ ,  $m = 0$ ,  $n_R = 1/2$  for laminar flow, one can obtain from Eq. (3.45) for  $A_c$

$$A_c (1 + \alpha^2)^{1/2} = 0.6159. \quad (3.52)$$

In the asymptotic case of  $Pr \rightarrow 0$ , Eq. (3.50) reduces to its asymptotic form, which looks for  $b_2 = 1$  identically to the solution derived in [3]

$$K_1 = 0.6159 Pr (2 + n_*) / (4 K_V). \quad (3.53)$$

Comparing Eq. (3.50) with the self-similar solution, Table 3.1, one can find the coefficients  $b_1$  and  $b_2$ . To satisfy Eq. (3.53),  $b_1$  must be finite and  $b_2 = 1$  at  $Pr \rightarrow 0$ . Let us set

$$b_2 = 1 + b_3 Pr^{n_{p1}}, b_1 = \text{const.}, b_3 = \text{const.} \quad (3.54)$$

The coefficients  $b_1$  and  $b_3$  are independent of the Prandtl number and are determined at  $Pr = 1$ . Further, exponents  $n_{p1}$  and  $n_p$  were found separately for every  $Pr$  number from Table 3.1. In this procedure, the coefficient  $K_1$  from the self-similar solution has been substituted into Eq. (3.50) for  $n_* = 0$  and  $n_* = 2$ . Finally, we obtained [29]

**Table 3.8** Values of  $n_p$  and  $n_{p1}$  depending on the Prandtl number [1, 29, 30]

$Pr$	0.9	0.8	0.72	0.71	0.6	0.5	0.4	0.3	0.2	0.1	0.01
$n_p$	0.7290	0.7349	0.7436	0.7435	0.7529	0.7608	0.7721	0.7860	0.8036	0.8338	0.9156
$n_{p1}$	0.9349	0.9354	0.9316	0.9334	0.9366	0.9439	0.9519	0.9602	0.9765	0.9893	0.999

$$b_1 = 0.6827, \quad b_3 = 0.5939, \tag{3.55}$$

whereas the values of the exponents are listed in Table 3.8.

For computational purposes, the exponents  $n_{p1}$  и  $n_p$  were described as polynomials

$$n_{p1} = \sum_0^7 a_i Pr^i, \quad n_p = \sum_0^7 c_i Pr^i, \tag{3.56}$$

where  $a_0 = 1, a_1 = -0.008073, a_2 = -0.3558, a_3 = 0.5485, a_4 = 1.799, a_5 = -6.432, a_6 = 7.354, a_7 = -2.915, c_0 = 0.925, c_1 = -1.171, c_2 = 3.532, c_3 = -3.376, c_4 = -5.725, c_5 = 15.59, c_6 = -12.28, c_7 = 3.208.$

The coefficient  $K_1$  computed by Eq. (3.50) is presented in Table 3.9. It diverges from the self-similar solution, Table 3.1, by maximum 3.1 % (for  $n_* = -1.5$  and  $Pr = 1$ ); the errors become negligible for  $Pr \leq 0.1$  [1, 29, 30].

On both sides of Eq. (3.43), the exponents for the  $r$ -coordinate must be the same, which yields the expression  $1 + m + n_* = 1$  for  $q_w = \text{const}$ . For laminar flow,  $m = 0$ , hence,  $n_* = 0$ . Therefore, the Nusselt number for laminar flow for  $q_w = \text{const}$ . is exactly the same as that for  $T_w = \text{const}$ . In turbulent flow, as shown above,  $n_* = -m$  for  $q_w = \text{const}$ .

To conclude, as can be seen from Fig. 3.14, the exact and approximate solutions for air ( $Pr = 0.72$ ) are in good agreement with each other as well as with experimental results.

**Table 3.9** Values of the constant  $K_1$  by Eqs. (3.50) and (3.54)–(3.56) [1]

$Pr$	$n_* = -2$	$n_* = -1.5$	$n_* = -1$	$n_* = -0.5$	$n_* = 0$	$n_* = 1$	$n_* = 2$	$n_* = 3$	$n_* = 4$
1.0	0.0	0.1261	0.2311	0.3199	0.3961	0.5197	0.6159	0.6928	0.7557
0.72	0.0	0.1019	0.1887	0.2635	0.3286	0.4365	0.5223	0.5921	0.6500
0.71	0.0	0.1009	0.187	0.2612	0.3259	0.4332	0.5185	0.5880	0.6457
0.5	0.0	0.0788	0.1477	0.2084	0.2623	0.3539	0.4287	0.4910	0.5437
0.1	0.0	0.0204	0.0399	0.0586	0.0766	0.1104	0.1417	0.1707	0.1977
0.01	0.0	0.00219	0.00438	0.00655	0.00871	0.01301	0.01726	0.02148	0.02565

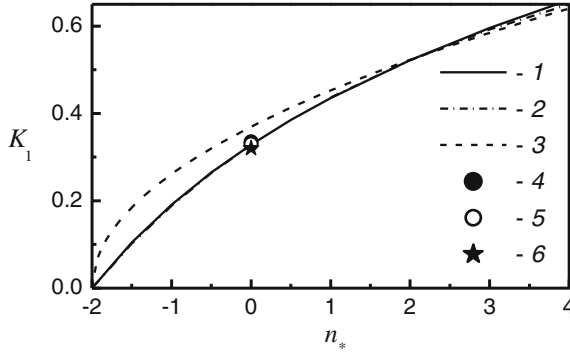


**Fig. 3.14** Effect of the exponent  $n_*$  on the constant  $K_1$  in Eq. (3.4) for laminar flow at  $Pr = 0.72$  [1]. 1—Exact solution [29, 30], 2—Eq. (3.50), 3—Eq. (3.6). Experiments for  $n_* = 0$ : 4—0.335 [6, 18, 22], 5—0.33 [15, 17, 23], 6—0.32 [16]

## 3.5 Finding a Wall Temperature Distribution for Arbitrary Nusselt Numbers

### 3.5.1 Solution of the Problem

Usually the thermal boundary layer equation is solved as a direct problem of searching the Nusselt number at a given wall temperature, Eq. (2.30), or in a modified form

$$\overline{\Delta T} = x^{n_*}, \quad (3.57)$$

where  $\overline{\Delta T} = \Delta T / \Delta T_{x=1}$  is the relative non-dimensional temperature difference on a surface.

The solution for the Nusselt number (3.4) found in such a way can be rewritten as

$$\begin{aligned} Nu &= K_1 Re_\phi^{(n+1)/(3n+1)} x^{2(n+1)/(3n+1)} \\ &= K_1 Re_\phi^{(n+1)/(3n+1)} x^{1+m}, \quad 2(n+1)/(3n+1) = 1+m. \end{aligned} \quad (3.58)$$

An inverse problem searches for a distribution of  $\Delta T$ , if the Nusselt number is given

$$Nu = K_1 Re_\phi^{(n+1)/(3n+1)} x^{m_x}, \quad Nu_b = K_1 Re_\phi^{(n+1)/(3n+1)} x^{m_x-1}, \quad (3.59)$$

where  $m_x = \text{const.}$  is an arbitrarily selected exponent not equal to  $1+m$  as in Eq. (3.58). An application in practice is e.g. a transient technique of experimental

finding of time-independent Nusselt numbers, whereas the measured distributions of  $\Delta T$  are unsteady. Here a steady-state distribution of  $\Delta T$  may be found only via solving an inverse problem.

To solve this problem [1, 92], the thermal boundary layer Eq. (3.43) in the integral form can be transformed to

$$\frac{d}{dx} [Re_\omega \bar{\delta} K_H K_m \overline{\Delta T}] = \frac{Nu}{Pr} \overline{\Delta T}. \quad (3.60)$$

Equation (2.77) can be presented in the form valid for laminar and turbulent flow

$$\bar{\delta} = C_\delta^* x^m, \quad C_\delta^* = \gamma Re_\omega^{-2n/(3n+1)}. \quad (3.61)$$

To remind, in laminar flow  $m = 1$  and  $K_m \bar{\delta} = I_\infty \alpha Re_\omega^{-1/2}$  [see Eq. (3.44)]. Equation (2.52) can be used to evaluate the Reynolds analogy parameter  $\chi$

$$\chi = \frac{Nu}{\frac{C_\gamma}{2} Re_\omega (1 + \alpha^2)^{1/2} Pr} = C_\chi x^{m_x - m - 1}, \quad (3.62)$$

$$C_\chi = \frac{K_1}{A_c (1 + \alpha^2)^{1/2} Pr}. \quad (3.63)$$

Let us use the notation

$$m_x^* = m_x - m. \quad (3.64)$$

In terms of Eq. (3.64), one can make sure that Eq. (3.58) holds at  $m_x^* = 1, m_x = 1 + m$ .

In view of Eqs. (3.62)–(3.64), one can rewrite Eq. (3.48) such as

$$K_H = a_* + b_* x^{m_x^* - 1}, \quad (3.65)$$

$$a_* = \frac{1}{b_2}, \quad b_* = -Pr^{n_p} (1 - K_V) \frac{b_1}{b_2} C_\chi. \quad (3.66)$$

An integration of Eq. (3.60) in view of Eqs. (3.61)–(3.66) yields [1]

$$\overline{\Delta T} = \frac{a_* + b_*}{a_* + b_* x^{m_x^* - 1}} x^{-2-m} \left[ \left( \frac{a_* x^{1-m_x^*} + b_*}{a_* + b_*} \right)^{\frac{1}{1-m_x^*}} x^{-1} \right]^{-\frac{K_1}{Pr K_m \gamma b_*}} \quad (3.67)$$

$$\overline{\Delta T} = \left[ \frac{K_H}{K_{H_{x=1}}} \right]^{-\frac{K_1}{Pr K_m \gamma b_* (1-m_x^*) - 1}} x^{-2-m}. \quad (3.68)$$

### 3.5.2 The Limiting Case of the Solution

For  $m_x^* \rightarrow 1$ , Eq. (3.68) degenerates to [1]

$$\overline{\Delta T} = x^{\frac{K_1}{PrK_m\gamma(a_*+b_*)} - 2 - m}. \quad (3.69)$$

Equations (3.57) and (3.69), being combined and transformed, yield

$$n_* = \frac{K_1}{PrK_m\gamma(a_* + b_*)} - 2 - m. \quad (3.70)$$

Specifying the value of  $n_*$  and keeping in mind that  $a_* + b_* = K_H$  at  $m_x^* = 1$ , one can obtain Eq. (3.50) for  $K_1$  valid under the conditions (2.30) or (3.57). In doing so, Eq. (3.57) can be treated as a specific case of Eq. (3.68) at  $m_x^* = 1$ .

### 3.5.3 Properties of the Solution for the Temperature Difference on the Wall

The point of extremum  $x_{\text{ext}}$  of the Eq. (3.68) for  $\overline{\Delta T}$  is located at [1, 93]

$$x_{\text{ext}} = \left[ \frac{\frac{K_1}{PrK_m\gamma} - b_*(m_x + 1)}{a_*(2 + m)} \right]^{\frac{1}{1 - m_x^*}}. \quad (3.71)$$

Expression  $\chi = \Delta^{-n} Pr^{-n_p}$  and Eq. (3.62) for the Reynolds analogy parameter  $\chi$  yield a relation for the normalized thermal boundary layer thickness  $\Delta$  [1]

$$\Delta = (\chi Pr^{n_p})^{-1/n} = (C_\chi x^{m_x^* - 1} Pr^{n_p})^{-1/n} = (C_\chi Pr^{n_p})^{-1/n} x^{(1 - m_x^*)/n}. \quad (3.72)$$

For the boundary condition (3.57) with  $m_x^* = 1$ , Eq. (3.72) results in the relation  $\Delta = \text{const}$ . The function  $\Delta(x)$  is increasing or decreasing at  $m_x^* < 1$  or  $m_x^* > 1$ , respectively.

In view of its physical nature, parameter  $K_H$  may be only positive. Equation (3.65) for  $K_H$  exhibits a limiting point where  $K_H = 0$ , whose parameters are

$$\chi_{\text{crit}} = \frac{1}{b_1 Pr^{n_p} (1 - K_V)}, \quad (3.73)$$

$$\Delta_{\text{crit}} = (\chi_{\text{crit}} Pr^{n_p})^{-1/n} = \left[ \frac{1}{b_1 (1 - K_V)} \right]^{-1/n}, \quad (3.74)$$

$$x_{\text{crit}} = \left[ \frac{\chi_{\text{crit}}}{C_\chi} \right]^{1/(m_x^* - 1)}. \quad (3.75)$$

Equations (3.71)–(3.75) can be used in the analysis of the behavior of  $\overline{\Delta T}$ .

### 3.5.4 Analysis of the Solution

The novel solution described above in Sect. 3.5 holds for a much wider range of thermal boundary conditions at the wall and incorporates previously known solutions as a specific case, provided that one of the parameters degenerates to unity [1, 92].

Indeed, Eq. (3.67) [or (3.68)] for the temperature difference and Eq. (3.59) for the Nusselt number contain two independent parameters:  $K_1$  and  $m_x$ . At  $m_x = 1 + m$  (or  $m_x^* = 1$ ), Eqs. (3.67), (3.68) and (3.59) reduce to the known Eq. (3.57) for  $\overline{\Delta T}$  and Eq. (3.58) [or (3.4)] for  $Nu$  with only one independent parameter:  $K_1$  or  $n_*$ . Equations (3.57), (3.67) and (3.68) for  $\overline{\Delta T}$  do not depend on the Reynolds number  $Re_\phi$ .

Both one-parameter Eq. (3.58) [or (3.4)] and two-parameter Eq. (3.59) represent monotonic distributions of the Nusselt number, i.e. the sign of the derivative  $dNu/dx$  is constant over the entire range of variation of the radial coordinate  $x$ .

At  $m_x^* = 1$ , the sign of the derivative  $d\overline{\Delta T}/dx$  in Eq. (3.57) is also constant. On the contrary, at  $m_x^* \neq 1$ , functions of  $\overline{\Delta T}$  given by Eq. (3.67) or (3.68) are non-monotonic and enable predicting curves of  $\overline{\Delta T}$  exhibiting points of maxima and minima.

**Application to laminar flow.** For validation of the model, experiments [94–96] (laminar air flow for  $Re_\phi = 53500$ ,  $Pr = 0.71$ ) were chosen. Let us assume that the temperature difference  $\overline{\Delta T}$  is determined by one-parameter Eq. (3.57) at  $n_* = -1$ , while the Nusselt number  $Nu_b$  is constant and determined by Eq. (3.58) with  $K_1 = 0.187$  (here  $m = 0$ ,  $m_x^* = m_x$ ).

Setting the value  $K_1 = 0.187$  and replacing  $m_x = 1$  by  $m_x = 0.6$  in Eq. (3.59) yields a radial dependence for  $Nu_b$  starting at infinity at  $x \rightarrow 0$  and further monotonically subsiding (curve 1 in Fig. 3.15). Based on Eq. (3.68), the temperature difference  $\overline{\Delta T}$  is a non-linear function of the coordinate  $x$  being zero at  $x = 0$ , having a maximum  $\overline{\Delta T} = 2.55$  at  $x \approx 0.2$  and further diminishing as a function similar to  $x^{-1}$  (curve 1 in Fig. 3.16). Obviously,  $\overline{\Delta T} = 1$  at  $x = 1$ . At the point of maximum, Eqs. (3.73)–(3.75) hold.

If  $n_* = 2$  in Eq. (3.57), the function  $\overline{\Delta T}(x)$  is increasing; at the same time, the Nusselt number  $Nu_b$  is constant with  $K_1 = 0.5185$  (and  $m_x = 1$ ). Provided that  $K_1 = 0.5185$  and  $m_x = 1.6$  in Eq. (3.59), the function  $Nu_b(x)$  is monotonically increasing.

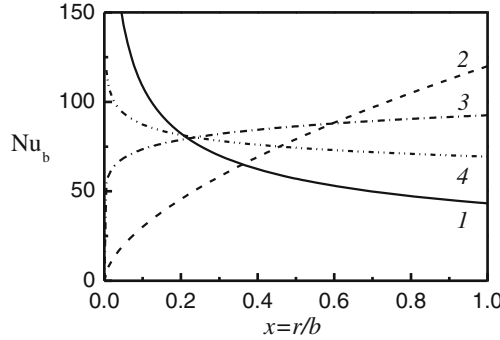


**Fig. 3.15** Radial distribution of the Nusselt number  $Nu_b$  by Eq. (3.59) for laminar flow ( $m = 0$ ) at  $Re_\varphi = 53,500$ ,  $Pr = 0.71$  [1]. 1— $m_x = 0.6$ ,  $K_1 = 0.187$ ; 2— $m_x = 1.6$ ,  $K_1 = 0.5185$ ; 3— $m_x = 1.1$ ,  $K_1 = 0.4$ ; 4— $m_x = 0.9$ ,  $K_1 = 0.3$

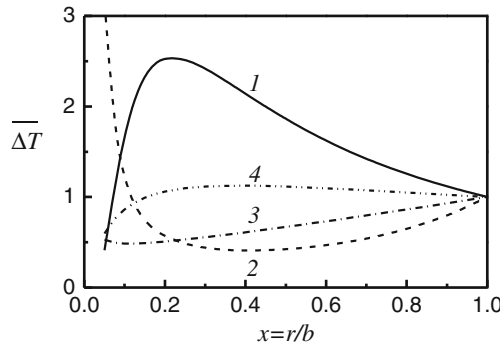


**Fig. 3.16** Radial distribution of the temperature difference  $\overline{\Delta T} = (T_w - T_\infty)/(T_w - T_\infty)_{x=1}$  by Eq. (3.68) for laminar flow ( $m = 0$ ) at  $Re_\varphi = 53500$ ,  $Pr = 0.71$  [1]. 1— $m_x = 0.6$ ,  $K_1 = 0.187$ ; 2— $m_x = 1.6$ ,  $K_1 = 0.5185$ ; 3— $m_x = 1.1$ ,  $K_1 = 0.4$ ; 4— $m_x = 0.9$ ,  $K_1 = 0.3$

Given this combination of  $K_1$  and  $m_x$ , the temperature difference decreases from  $\overline{\Delta T} \rightarrow \infty$  and reaches a point of minimum at  $x \approx 0.4$  with  $\overline{\Delta T} = 0.4075$ . Further at  $x > 0.4$ , the function  $\overline{\Delta T}$  demonstrates a trend of increase as a function similar to  $x^2$ .

Curves 3 and 4 in Figs. 3.15 and 3.16 were plotted to outline the heat transfer regimes situated between the cases 1 and 2 discussed above.

**Application to turbulent flow.** For our analysis, we selected the experiments [86, 87], while the equality  $n = n_T$  was always held while using Eqs. (3.59) and (3.68) [93, 97]. The results of simulations for the case  $n_* = 0.1$  (performed at  $n = n_T = 1/6$ ) are shown in Figs. 3.17 and 3.18. In the region  $x \approx 0.3-0.85$ , an approximation  $\overline{\Delta T} = c_{0*}x^{n_*}$  at  $n_* = 0.06$ ,  $c_{0*} = 1.16$  for  $Re_\varphi = (1.08-1.35) \times 10^6$  and at  $n_* = 0.06$ ,  $c_{0*} = 1.26$  for  $Re_\varphi = (2.14-3.2) \times 10^6$  locally correlates with experimentally measured function  $\overline{\Delta T}$ .

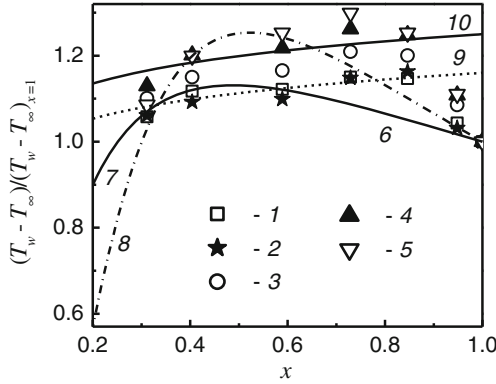


**Fig. 3.17** Radial variation of the temperature difference  $\overline{\Delta T}$  for  $Pr = 0.72$ , case conventionally  $n_* = 0.1$  [1]. Experiments [87]: 1— $Re_\varphi = 1.08 \times 10^6$ ; 2— $1.6 \times 10^6$ ; 3— $1.88 \times 10^6$ ; 4— $2.14 \times 10^6$ ; 5— $3.2 \times 10^6$ . Calculations by Eq. (3.68) for  $n = 1/6$ : 6— $K_1 = 0.0232$  and  $m_x = 1.48$ ; 7—0.0229 and 1.43; 8—0.0224 and 1.38. Approximation  $\overline{\Delta T} = c_{0*}x^{n_*}$ : 9— $c_{0*} = 1.16$  and  $n_* = 0.06$ ; 10— $c_{0*} = 1.25$  and  $n_* = 0.06$

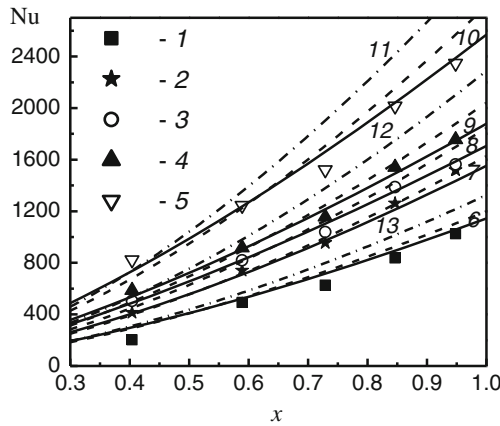


**Fig. 3.18** Radial variation of the Nusselt number, case conventionally  $n_* = 0.1$  [1]: 1–5—experiments [87]; 6–11—calculations by Eqs. (3.58) and (3.59) for  $n = n_T = 1/6$ . Solid lines, Eq. (3.59): 6, 7— $K_1 = 0.0232$ ,  $m_x = 1.48$ ; 8–10— $K_1 = 0.0224$ ,  $m_x = 1.38$ . Dashed lines 6–10—Eq. (3.58),  $K_1 = 0.0232$ ,  $n_R = 0.778$ ,  $m_x = 1.556$ . Dash-dotted lines 11–13—Dorfman’s Eq. (3.21) for  $n_* = 0.1$ . 1, 6, 13— $Re_\varphi = 1.08 \times 10^6$ ; 2, 7— $1.6 \times 10^6$ ; 3, 8— $1.88 \times 10^6$ ; 4, 9, 12— $2.14 \times 10^6$ ; 5, 10, 11— $3 \times 10^6$

As a result, calculations by Eq. (3.58) [with  $K_1$  given by Eq. (3.34)] agree well with measured Nu numbers over the same range of  $x$  (here the exact value  $c_{0*}$  is unimportant).

At the same time, for  $x > (0.7-0.85)$  experimental temperature difference  $\overline{\Delta T}$  diminishes, while the predicted  $\overline{\Delta T}$  continues increasing. Owing to this, predicted

Nusselt numbers surpass the experimental data. This tendency becomes more noticeable at larger Reynolds numbers  $Re_\phi$ . Dorfman's Eq. (3.21) at  $n_* = 0.1$ ,  $n = n_T = 1/7$  (see curves 11–13 in Fig. 3.18 and explanations to them) diverges from experiments even more noticeably.

Using Eq. (3.59) for the Nusselt number, Fig. 3.18, and Eq. (3.68) for  $\overline{\Delta T}$  can provide a better agreement between simulations and experiments (see Fig. 3.17). While Eq. (3.57) ensures a positive sign of  $d\overline{\Delta T}/dx$  for any  $x$ , Eq. (3.68), on the contrary, enables rather flexible modeling of the sign of the derivative  $d\overline{\Delta T}/dx$ , which changes here from “plus” to “minus” with increasing  $x$ . This ensures a more close agreement between the computed and measured values of the Nusselt number (Fig. 3.18).

Predictions for the case  $n_* = -0.2$  (performed for  $n = n_T = 1/6$ ) are depicted in Figs. 3.19 and 3.20. A fair consistency of the computed and measured functions of  $\overline{\Delta T}$  is evident for  $x \geq 0.6$  (Fig. 3.19). Qualitative agreement of the sign of the predicted and measured function  $d\overline{\Delta T}/dx$  demonstrates only curve 4 over the range  $x = 0.35$ – $0.45$ . Important is that the approximation  $\overline{\Delta T} = c_{0*}x^{n_*}$  correlates with the experiments for  $x > 0.6$  only for  $n_* = -1.5$  (and  $c_{0*} = 1.14$ ), though the value suggested in [86, 87] is  $n_* = -0.2$  (curve 6).

The Nusselt numbers in Fig. 3.20 were computed for two different values of the Reynolds numbers. Experimental data 1 and *upper lines* 3–6 relate to the value  $Re_\phi = 2.65 \times 10^6$ , whereas experiments 2 and *lower lines* 3–6 correspond to  $Re_\phi = 1.08 \times 10^6$ . Curves for the  $Nu$  number depend noticeably on the values for  $K_1$  and  $m_x$ .

The lower curve 4 of the  $Nu$  number in Fig. 3.20 computed by Eq. (3.58) for  $Re_\phi = 1.08 \times 10^6$  conforms to the experiments 2. Nevertheless, at  $x \approx 0.4$  the flow is laminar, thus an agreement with it testifies that the computed curve 4 lies lower than

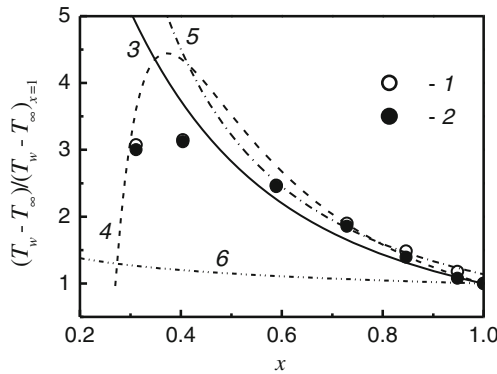


**Fig. 3.19** Radial variation of the temperature difference  $\overline{\Delta T} = (T_w - T_\infty)/(T_w - T_\infty)_{x=1}$  for  $Pr = 0.72$ ,  $n_* = -0.2$  [1]. Experiments [87]: 1— $Re_\phi = 1.08 \times 10^6$ ; 2— $2.65 \times 10^6$ . Calculations by Eq. (3.68) for  $n = 1/6$ : 3— $K_1 = 0.0157$ ,  $m_x = 1.3$ ; 4— $K_1 = 0.0137$ ,  $m_x = 0.775$ . Approximation  $\overline{\Delta T} = c_{0*}x^{n_*}$ : 5— $c_{0*} = 1.14$ ,  $n_* = -1.5$ ; 6— $c_{0*} = 1.0$ ,  $n_* = -0.2$

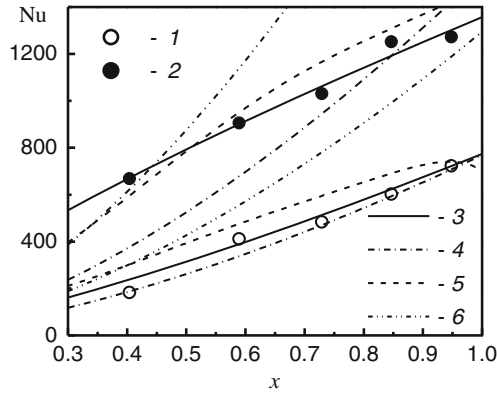


**Fig. 3.20** Variation of the Nusselt number,  $n_* = -0.2$  [1]: 1, 2—experiments [87]; 3–5—Eq. (3.58),  $n = n_T = 1/6$ ; 6—Dorfman's Eq. (3.21),  $n_* = -0.2$ . Lower lines 3–6 and symbol 1— $Re_\varphi = 1.08 \times 10^6$ ; upper lines 3–6 and symbol 2— $Re_\varphi = 2.65 \times 10^6$ . Lower line 3—Eq. (3.59),  $K_1 = 0.0157$ ,  $m_x = 1.3$ ; upper line 3—Eq. (3.59),  $K_1 = 0.0137$ ,  $m_x = 0.775$ . Lines 4—Eq. (3.58),  $K_1 = 0.0156$ ,  $n_R = 0.778$ ,  $m_x = 1.556$ ,  $n_* = -1.5$ . Lines 5—numerical modelling (see Fig. 3.13)

it should be expected. Therefore, for  $Re_\varphi = 2.65 \times 10^6$  experimental points 1 significantly exceed the upper curve 4 at  $x \leq 0.7$ , where turbulent flow is developed.

Using Eq. (3.59) with  $\overline{\Delta T}$  predicted by Eq. (3.68), one can attain a good agreement with the experiments for the Nu number, if the coefficients  $K_1$  and  $m_x$  are properly selected.

Dorfman's Eq. (3.21) at  $n_* = -0.2$  predicts much too high Nusselt numbers as compared to the experimental data (curves 6 in Fig. 3.20).

Predictions and measurements for  $n_* = 0.4$  and  $n_* = 0.6$  are depicted in Figs. 3.21 and 3.22. Values  $n = n_T = 1/6.5$  and  $n = n_T = 1/6$  were used for  $Re_\varphi = 1.59 \times 10^6$  and  $2.67 \times 10^6$ , accordingly. The value  $n_* = 0.6$  in Eq. (3.57) indeed conforms to the experiments at  $x = 0.3$ – $0.6$  and  $Re_\varphi = 1.59 \times 10^6$  (Fig. 3.21). However, experiments for  $Re_\varphi = 2.67 \times 10^6$  can be better simulated with  $n_* = 0.7$  rather than with  $n_* = 0.4$  [87].

In addition, Eq. (3.68) ensures a variation of the absolute value of  $d\overline{\Delta T}/dx$  in the radial direction and a wide range of selection of the parameters  $K_1$  and  $m_x$  (Fig. 3.21).

The local Nusselt numbers in Fig. 3.22 show that Eqs. (3.59) and (3.68) with carefully selected values  $K_1$  and  $m_x$  enable a better agreement with experiments than Eqs. (3.57) and (3.58), which can be seen for the larger value  $Re_\varphi = 2.67 \times 10^6$ . As the curves 6 and 7 in Fig. 3.22 prove, the deviation of the Dorfman's Eq. (3.21) is not significant.

Thus, Eqs. (3.59) and (3.68) essentially expand the possibilities for analytical predictions of heat transfer over a rotating disk subject to arbitrary thermal boundary conditions.

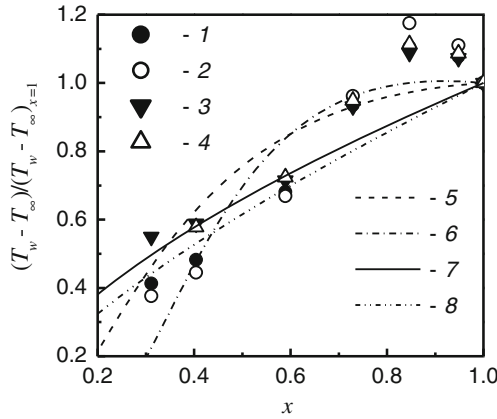


**Fig. 3.21** Radial variation of the temperature difference  $\overline{\Delta T} = (T_w - T_\infty) / (T_w - T_\infty)_{x=1}$  for  $Pr = 0.72$ , cases  $n_* = 0.4$  (data 1, 2, 6, 8) and  $n_* = 0.6$  (data 3, 4, 5, 7) [1]. Experiments [87]: 1— $Re_\phi = 2.67 \times 10^6$ ; 2— $3.14 \times 10^6$ ; 3— $0.615 \times 10^6$ ; 4— $1.71 \times 10^6$ . Calculations by Eq. (3.68): 5— $K_1 = 0.0219$ ,  $m_x = 1.48$ ,  $n = 1/6.5$ ; 6— $K_1 = 0.0249$ ,  $m_x = 1.34$ ,  $n = 1/6$ . Calculations by Eq. (3.57): 7— $n_* = 0.6$ , 8— $n_* = 0.7$

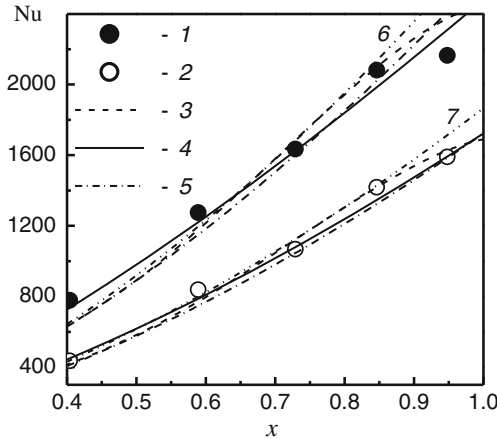


**Fig. 3.22** Radial variation of the Nusselt number [1]. 1, 2—experiments [87]. 3—numerical modelling (Fig. 3.12). Case  $n_* = 0.4$  (upper group of lines,  $Re_\phi = 2.67 \times 10^6$ ), calculations at  $n = n_T = 1/6$ : 4—Eq. (3.59),  $m_x = 1.34$ ,  $K_1 = 0.0249$ ; 5—Eq. (3.58),  $n_* = 0.7$ ,  $K_1 = 0.0262$ ,  $n_R = 0.778$ ,  $m_x = 1.556$ . Case  $n_* = 0.6$  (lower group of lines,  $Re_\phi = 1.59 \times 10^6$ ), calculations at  $n = n_T = 1/6.5$ : 4—Eq. (3.59),  $m_x = 1.48$ ,  $K_1 = 0.0219$ ; 5—Eq. (3.58),  $m_x = 1.58$ ,  $K_1 = 0.02265$ ,  $n_R = 0.7896$ ,  $n_* = 0.6$ . Line 6—Dorfman's Eq. (3.21),  $n_* = 0.4$ ; line 7—Eq. (3.21),  $n_* = 0.6$

### 3.6 Theory of Local Modelling

The bedrock of the theory of local modelling is Eq. (2.51) at  $M_s = \text{const.}$  and  $n_* = 2$  (see Sect. 2.3.2), which results in the Dorfman's solutions (3.6) and (3.21). An improvement of this model can be attained via setting a variable value of  $M_s$  dependent on the parameter  $n_*$  [1]. Let us rewrite the thermal boundary layer Eq. (3.60) such as

$$\frac{1}{\Delta T} \frac{d}{dr} [Re_T^{**} r \Delta T] = Nu/Pr. \quad (3.76)$$

Let us further substitute Eq. (2.51) and boundary condition (2.30) into Eq. (3.76). As a result, the Nusselt number can be expressed as

$$Nu = M_s^{\frac{1}{1+\sigma}} (2n_R + n_* + 1)^{\frac{\sigma}{1+\sigma}} (1 + \alpha^2)^{\frac{1}{2(1+\sigma)}} Re_\omega^{\frac{1}{1+\sigma}} Pr^{\frac{1+\sigma-n_*}{1+\sigma}}. \quad (3.77)$$

We wish to elucidate just the basic features of the theory; hence, listed below are the solutions for only a single value  $Pr = 0.72$ . As a result, Eq. (3.34), together with the equations for  $M_s$  and  $St$  for *turbulent flow* ( $n = 1/7$ ) can be written as

$$\frac{1}{K_1} = 34.99 + \frac{48.33}{2.6 + n_*}, \quad (3.78)$$

$$M_s = \frac{1.252}{(34.99 + 48.33/(2.6 + n_*))^{1.25} (2.6 + n_*)^{0.25}}, \quad (3.79)$$

$$St = \frac{1.475 \cdot Re_T^{** - 0.25}}{(34.99 + 48.33/(2.6 + n_*))^{1.25} (2.6 + n_*)^{0.25}}. \quad (3.80)$$

For *laminar flow*, the constant  $K_1$  given by Eq. (3.50) and the Stanton number for  $Pr = 0.72$  can be expressed as

$$K_1 = \frac{0.4435}{0.3486 + 2.002/(2 + n_*)}, \quad (3.81)$$

$$St = \frac{0.2922 \cdot Re_T^{** - 1.0}}{(2 + n_*)(0.3486 + 2.002/(2 + n_*))^2}. \quad (3.82)$$

To conclude, Eqs. (3.80) and (3.82) essentially improve agreement with experiments, however, at the expense of ignoring the basic postulate of the theory:  $M_s = \text{const.}$  The mathematical formulation of Eqs. (3.80) and (3.82) was suggested in analogy to Eq. (3.34) obtained by means of a fundamentally different theoretical model.

## 3.7 Unsteady Heat Transfer

### 3.7.1 Transient Experimental Technique

Thermochromic liquid crystals are used for experimental measurements of steady-state heat transfer rate over a surface using a transient technique. The following physical phenomenon lies behind this technique: after a short time from the onset of unsteady heating/cooling, the heat transfer coefficient accepts a time-independent value equivalent to that for steady-state heat transfer subject to identical thermal boundary conditions.

Experimental data reduction operates by employing a one-dimensional heat conduction solution for a semi-infinite wall subject to a convective boundary condition for a step change in the fluid temperature  $T_\infty$  [98–105]

$$F_t(t) = \frac{T_w(t) - T_\infty}{T_{w,i} - T_\infty} = \exp(\gamma^2) \cdot \operatorname{erfc}(\gamma), \quad \gamma = \alpha\sqrt{a_w t}/\lambda_w \quad (3.83)$$

where  $T_{w,i}$  and  $T_\infty$  are constants;  $a_w$  and  $\lambda_w$  denote the thermal diffusivity and conductivity of the body, accordingly. Given a measured curve of the surface temperature  $T_w(t)$ , Eq. (3.83) can be solved to find the heat transfer coefficient  $\alpha$ . The semi-infinite-plate model holds, if conduction heat transfer does not penetrate deeply into the body.

A solution for a plate with a thickness  $s$  having identical heat transfer coefficients at both sides [13, 106] replaces Eq. (3.83), if a plate is relatively thin

$$F_t(t) = \vartheta(t, y = 1), \quad \vartheta(t, y) = \sum_{m=1}^{\infty} E_m \cos(\mu_m y) \exp(-\mu_m^2 \text{Fo}), \quad (3.84)$$

$$E_m = \frac{2 \sin(\mu_m)}{\mu_m + \sin(\mu_m) \cos(\mu_m)}, \quad \cot(\mu_m) = \mu_m / \text{Bi}, \quad (3.85)$$

where Eq. (3.85) defines eigenvalues  $\mu_n$ ;  $\vartheta(t, y) = (T(t, y) - T_\infty)/(T_{w,i} - T_\infty)$ ;  $y = z/(0.5s)$ .

It will be shown below that the transient technique for measurements of surface heat transfer coefficients described above can be applied for a Plexiglas<sup>®</sup> disk subject to even very strongly non-uniform initial temperature distribution. A disk made of aluminium is not usable for this purpose [1], because of strong radial heat conduction effects.

### 3.7.2 Self-similar Equations for Unsteady Convective Heat Transfer

Self-similar functions and independent variables for unsteady heat transfer in stationary flow over a rotating disk were obtained in [1, 107, 108]. As a result, Eq. (2.12) of the thermal boundary layer and the boundary condition (2.29) take the form

$$\theta'' = Pr[g_*\theta + \theta'(H - \eta/2) + n_*F\theta], \quad (3.86)$$

$$\eta = z / (vt)^{1/2}, H(\eta) = v_z(t/v)^{1/2} \quad (3.87)$$

$$g_* = \frac{t}{F_t} \frac{dF_t}{dt}, \quad (3.88)$$

$$\theta = 1 \text{ for } \eta = 0 \text{ and } \theta = 0 \text{ for } \eta \rightarrow \infty. \quad (3.89)$$

Here primes denote derivatives with respect to the similarity variable  $\eta$ .

The solution of Eq. (3.86) requires specifying the function  $H(\eta)$ . For this purpose, the time-independent Eqs. (2.32)–(2.35) (for  $N = 0$ ,  $\beta = 0$ ) must be non-dimensionalized and solved with respect to the similarity variable  $\eta$  instead of  $\zeta = z\sqrt{\omega/v}$ . As a result, at the non-dimensionalization of the velocity components and the static pressure in Eq. (2.26), parameter  $1/t$  replaces the angular velocity  $\omega$

$$F(\eta) = v_r r/t, G(\eta) = v_\phi t/r, \text{ and } P(\eta) = -pt/(\rho v), \quad (3.90)$$

whereas Eqs. (2.32)–(2.35) and functions  $F$ ,  $G$ ,  $H$  and  $P$  still do not depend on time.

As soon as  $v_\phi = \omega r$  at  $z = 0$ , the new function  $G(\eta) = \omega t$  at  $\eta = 0$ . Therefore, the boundary conditions (2.27) and (2.28) can be finally rewritten to a new self-similar form

$$\eta = 0: \quad F = H = 0, \quad G = \omega t, \quad (3.91)$$

$$\eta \rightarrow \infty: \quad G = F = 0. \quad (3.92)$$

To calculate the Nusselt number  $Nu_b$ , the following relations are used

$$Nu_b = K_1 Re_\phi^{1/2}, \quad K_1 = - \left( \frac{d\theta}{d\zeta} \right)_{\zeta=0} = \frac{1}{\sqrt{\omega t}} \left( \frac{d\theta}{d\eta} \right)_{\eta=0}. \quad (3.93)$$

The new non-dimensional parametric variable  $\omega t$  arises in Eqs. (3.91) and (3.93).

Equations (3.87) and (3.90) were derived with the help of the group theory [90]. Authors of the work [31] employed self-similar functions almost identical to

Eqs. (3.87) and (3.90) with a difference to within a constant; however, this model was not formally grounded from the mathematical point of view.

### 3.7.3 Cooling of an Isothermal Rotating Disk

Mathcad software was used to numerically solve Eqs. (3.86) and (2.32)–(2.35) [in view of Eqs. (3.90)–(3.92)] for the condition  $T_w = \text{const.}$  (or  $n_* = 0$ ) [1, 107, 108].

Equation (3.88) with account for Eq. (3.83) transforms to

$$g_* = \gamma^2 - \gamma / (\pi^{1/2} F_t), \quad \gamma = K_1 Pr^{-1/2} (a_w/a)^{1/2} (\lambda/\lambda_w) \sqrt{\omega t}. \quad (3.94)$$

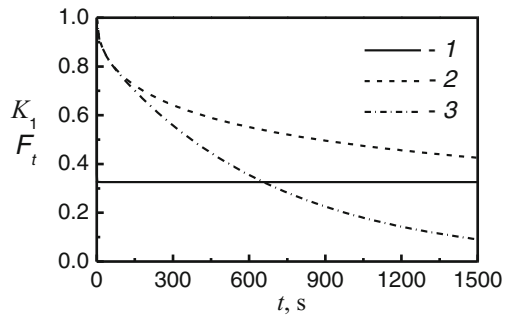
In simulations, physical properties and geometric parameters were: for Plexiglas® [96]  $\lambda_w = 0.19 \text{ W}/(\text{m}^2 \text{ K})$ ,  $a_w = 1.086 \times 10^{-7} \text{ m}^2/\text{s}$ ; for air [90]  $\lambda = 0.02624 \text{ W}/(\text{m}^2 \text{ K})$ ,  $a = 2.216 \times 10^{-5} \text{ m}^2/\text{s}$ ;  $Pr = 0.71$ ; thickness of the disk  $s = 0.01 \text{ m}$ ;  $Re_\varphi = 5.35 \times 10^4$  that means  $\omega = 52.36 \text{ 1/s}$  (500 r.p.m.) [96]. The value of  $K_1 = 0.326$  at  $T_w = \text{const.}$  was used in calculation of the Biot number in Eq. (3.84) and parameter  $\gamma$  that gives  $\gamma = 0.0768 \sqrt{\omega t}$ ,  $Bi = 0.395$ .

The constant  $K_1$ , together with the Nusselt number  $Nu_b$ , become very fast time-independent (see Fig. 3.23): at  $\omega t \approx 130$  or  $t \approx 2.5 \text{ s}$  (setting 1 % deviation from the steady-state as a threshold), whereas  $F_t(t) \approx 0.96$  [1]. The curves for  $K_1(t)$  predicted using Eqs. (3.83) and (3.84) practically coincide (see Fig. 3.23).

If heat transfer coefficients of an isothermal disk of a thickness  $s$  (Fig. 2.1) are identical at  $z = 0$  and  $z = -s$ , solution (3.84) testifies that already for  $Fo = 0.3$  (or  $t = 69 \text{ s}$ ) the function  $F_t(t)$  with an inaccuracy of 0.37 % is represented by just the first term of Eq. (3.84). In other words, a so-called regular regime of heat transfer [106] is established.

As seen in Fig. 3.23, during the initial time period, dimensionless surface temperatures  $F_t(t)$  calculated by Eqs. (3.83) and (3.84) practically coincide and start diverging at  $Fo = 0.456$ , when the process of cooling involves the entire thickness of the thin disk, which afterwards cools down much faster than the disk with a

**Fig. 3.23** Variation of  $K_1$  and  $F_t$  with time [1]. 1— $K_1$ ; 2— $F_t(t)$ , Eq. (3.83); 3— $F_t(t)$ , Eq. (3.84)



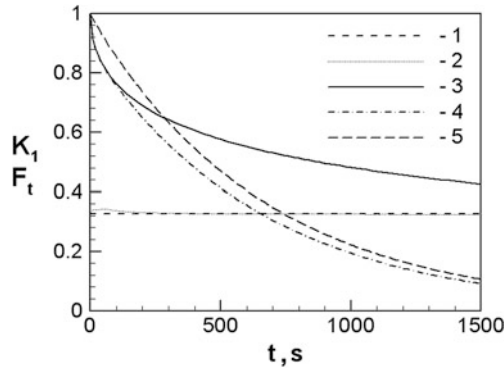


**Fig. 3.24** Variation of the parameters  $K_1$  and  $F_t$  in time according to the self-similar solution and simulations using the CFX-5 [111]. 1— $K_1$ , self-similar solution; 2— $K_1$ , CFX-5; 3— $F_t(t)$ , Eq. (3.83); 4— $F_t(t)$ , Eq. (3.84); 5— $F_t(t)$ , CFX-5

semi-infinite thickness. In [109, 110], this limiting Fourier number equals to 0.25 and 1.0, respectively.

The problem of unsteady cooling of a finite-thickness disk considered here was simulated also as a conjugate problem using the commercial CFD software CFX-5 [111]. The temporal curve of the cooling rate of the disk surface obtained from the CFD simulations and presented in Fig. 3.24 agrees rather well with that predicted by Eq. (3.84).

### 3.7.4 Unsteady Two-Dimensional Heat Conduction in a Non-uniformly Heated Disk

Differential equation of unsteady 2D heat conduction in the plate together with the boundary conditions can be written as [108]

$$\frac{\partial \vartheta}{\partial Fo} = \frac{1}{H^2} \left( \frac{\partial^2 \vartheta}{\partial x^2} + \frac{1}{x} \frac{\partial \vartheta}{\partial x} \right) + \frac{\partial^2 \vartheta}{\partial y^2}, \tag{3.95}$$

$$Fo = 0: \quad \vartheta = x^{n_*}, \tag{3.96}$$

$$x = 0: \quad \frac{\partial \vartheta}{\partial x} = 0, \quad x = 1: \quad \left( \frac{\partial \vartheta}{\partial x} \right)_{x=1} = -Bi_1 \vartheta_{x=1}, \tag{3.97}$$

$$y = 0: \quad \frac{\partial \vartheta}{\partial y} = 0, \quad y = 1: \quad \left( \frac{\partial \vartheta}{\partial y} \right)_{y=1} = -Bi_2 \vartheta_{y=1}, \tag{3.98}$$

where  $x = r/b$  and  $y = z/(0.5s)$ . In fact, Eq (3.96) is Eq. (2.30) reformatted with the help of the new variables. Here the Biot numbers  $Bi_1$  and  $Bi_2$  characterize convective heat transfer from the cylindrical and flat surfaces of the disk, respectively.

The method of separation of variables was used to solve Eqs. (3.95)–(3.98) analytically [108], where the final solution can be presented as

$$\vartheta(\text{Fo}, x, y) = \sum_{n=1}^{\infty} \sum_{m=1}^{\infty} D_n E_m J_0(\mu_{xn}x) \cos(\mu_{ym}y) \exp\left[-(\mu_{xn}^2/H^2 + \mu_{ym}^2)\text{Fo}\right], \quad (3.99)$$

$$D_n = \frac{{}_1F_2(1 + n_*/2; 1, 2 + n_*/2; -\mu_{xn}^2/4)/(2 + n_*)}{0.5[J_0^2(\mu_{xn}) + J_1^2(\mu_{xn})]}, \quad (3.100)$$

$$\frac{J_1(\mu_{xn})}{J_0(\mu_{xn})} = \frac{Bi_1}{\mu_{xn}}. \quad (3.101)$$

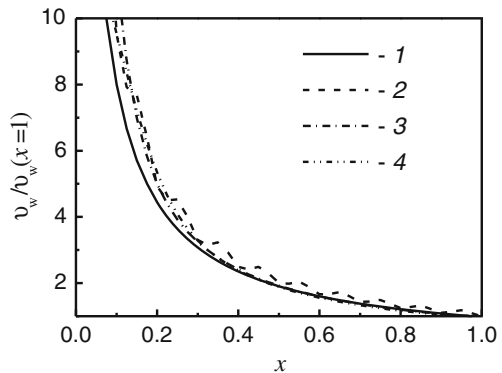
Here,  $E_m$  and  $\mu_{ym}$  are defined by Eq. (3.85);  $J_0$  and  $J_1$  are Bessel functions of the first kind and zero/first order, accordingly. Ignoring radial heat conduction, Eq. (3.99) simplifies to Eq. (3.84). In Eq. (3.100),  ${}_1F_2$  is a hypergeometric function of  $-\mu_{xn}^2/4$  [112].

Figures 3.25 and 3.26 depict radial variations of the disk temperature in cases with  $n_* = -1$  and  $2$ , where  $n_*$  is strongly different from zero. Figures 3.25 and 3.26 demonstrate that during cooling of a Plexiglas<sup>®</sup> disk the surface temperature  $\vartheta_w/\vartheta_w(x=1)$  in fact repeats the initial functions (3.96) over practically entire disk surface.

Strictly saying, Eq. (3.96) contradicts with the steady-state boundary conditions (3.97) for  $x = 0$  and  $x = 1$ . Hence, time-dependent distributions  $\vartheta_w/\vartheta_w(x=1)$  are distorted in the neighborhood of the locations  $x = 0$  and  $x = 1$ ; therefore the behavior of the heat transfer coefficient  $\alpha_{2,t}$  is studied within a region of  $x = 0.2$ – $0.9$ .

To conclude, the transient technique for measurements of surface heat transfer can be used together with a Plexiglas<sup>®</sup> disk subject to any initial temperature distribution.

**Fig. 3.25** Variation of the function  $\vartheta_w/\vartheta_w(x=1)$  with  $x$  according to Eq. (3.99) at  $n_* = -1$  [1]. 1—Eq. (3.96); 2— $\text{Fo} = 0.00652$ ; 3— $\text{Fo} = 0.869$ ; 5— $\text{Fo} = 2.607$



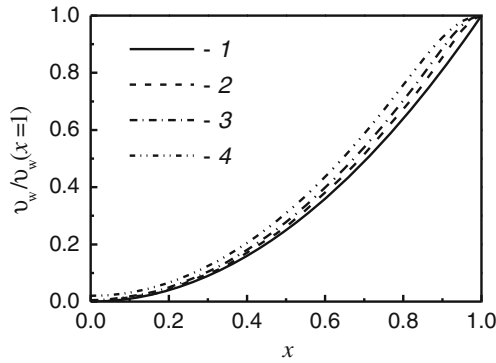


**Fig. 3.26** Variation of the function  $v_w/v_w(x=1)$  with  $x$  according to Eq. (3.99) at  $n_* = 2$  (dash-dotted lines) and  $n_* = 0.5$  (solid lines) for different values of Fo [1]. 1—Eq. (3.96); 2—Fo = 0.0261; 3—Fo = 0.261; 4—Fo = 0.869; 5—Fo = 2.607

## References

1. Shevchuk IV (2009) Convective heat and mass transfer in rotating disk systems. Springer, Berlin, Heidelberg
2. Dorfman LA (1963) Hydrodynamic resistance and the heat loss of rotating solids. Oliver and Boyd, Edinburgh, UK
3. Owen JM, Rogers RH (1989) Flow and heat transfer in rotating-disc systems. Volume 1: rotor-stator systems. Research Studies Press Ltd., Taunton, Somerset, England
4. Owen JM, Rogers RH (1995) Flow and heat transfer in rotating-disc systems Volume 2: rotating cavities. Research Studies Press Ltd., Taunton, Somerset, England
5. Schlichting G (1968) Boundary-layer theory. McGraw-Hill Book Company, New York
6. Elkins CJ, Eaton JK (1997) Heat transfer in the rotating disk boundary layer. Stanford University, Department of Mechanical Engineering, Thermosciences Division Report TSD-103. Stanford University, USA
7. Itoh M, Hasegawa I (1994) Turbulent boundary layer on a rotating disk in infinite quiescent fluid. JSME Int J Ser B 37(3):449–456
8. Lingwood RJ (1996) An experimental study of absolute instability of the rotating-disk boundary-layer flow. J Fluid Mech 314:373–405
9. Theodorsen Th, Regier A (1944) Experiments on drag of revolving discs, cylinders and streamline rods at high speeds. NASA Report No 793
10. Kempf G. (1924) Über Reibungswiderstand rotierender Scheiben. Vorträge auf dem Gebiet der Hydro- und Aerodynamik, Innsbrucker Kongress, 1922. Berlin, p 22
11. Schmidt W (1921) Ein einfaches Messverfahren für Drehmomente. Z VDI 65:411–444
12. Littel HS, Eaton JK (1994) Turbulence characteristics of the boundary layer on a rotating disk. J Fluid Mech 266:175–207
13. Elkins CJ, Eaton JK (2000) Turbulent heat and momentum transfer on a rotating disk. J Fluid Mech 402:225–253
14. Parthasarathy RN (2002) Analysis of the turbulent boundary layer on a rotating disk. Microsyst Technol 8(4–5):278–281
15. Bogdan Z (1982) Cooling of a rotating disk by means of an impinging jet. In: Proceedings of 7th IHTC heat transfer 1982, vol 3. Munich, Germany, pp 333–336

16. Chen Y-M, Lee W-T, Wu S-J (1998) Heat (mass) transfer between an impinging jet and a rotating disk. *Heat Mass Transfer* 34(2–3):101–108
17. Cobb EC, Saunders OA (1956) Heat transfer from a rotating disk. In: *Proceedings of the Royal Society A*, vol 236, pp 343–349
18. Janotková E, Pavelek M (1986) A naphthalene sublimation method for predicting heat transfer from a rotating surface. *Strojnícky časopis* 37(3):381–393 (in Czech)
19. Janotková E, Pavelek M (1993) Application of interferometry to temperature field measurements in neighbourhood of rotating discs. In: *Proceedings of 11th CHISA 93*. Paper No 0015, Prague, Czech Republic
20. Kreith F, Taylor JH, Chong JP (1969) Heat and mass transfer from a rotating disk. *Trans ASME J Heat Transfer* 81:95–105
21. Pavelek M, Janotková E (1989) Surface temperature calculation for applying naphthalene sublimation method on rotating disks. In: *Proceedings of 6th conference thermogrammetry thermal engineering*. Budapest, Hungary, pp 111–115
22. Pavelek M, Janotková E (1996) An experimental study of heat transfer from co-rotating disks. *Proceedings of 12th CHISA 96*, Paper G 8.48, Prague, Czech Republic
23. Popiel CO, Boguslawski L (1975) Local heat-transfer coefficients on the rotating disk in still air. *Int J Heat Mass Transfer* 18(1):167–170
24. Shimada R, Naito S, Kumagai S, Takeyama T (1987) Enhancement of heat transfer from a rotating disk using a turbulence promoter. *JSME Int J Ser B* 30(267):1423–1429
25. Sparrow EM, Chaboki A (1982) Heat transfer coefficients for a cup-like cavity rotating about its own axis. *Int J Heat Mass Transfer* 9(25):1334–1341
26. Shevchuk IV (2000) Turbulent heat transfer of rotating disk at constant temperature or density of heat flux to the wall. *High Temp* 38(3):499–501
27. Cardone G, Astarita T, Carlomagno GM (1996) Infrared heat transfer measurements on a rotating disk. *Opt Diagn Eng* 1(2):1–7
28. Cardone G, Astarita T, Carlomagno GM (1997) Heat transfer measurements on a rotating disk. *Int J Rotating Mach* 3(1):1–9
29. Shevchuk IV (2001) Effect of the wall temperature on laminar heat transfer in a rotating disk: an approximate analytical solution. *High Temp* 39(4):637–640
30. Shevchuk IV (2001) An improved enthalpy-thickness model for predicting heat transfer of a free rotating disk using an integral method. In: *Proceedings of 35th ASME NHTC'01*. Paper NHTC2001–20195, Anaheim, California, USA
31. Cheng W-T, Lin H-T (1994) Unsteady and steady mass transfer by laminar forced flow against a rotating disk. *Wärme und Stoffübertragung* 30(2):101–108
32. Lin H-T, Lin L-K (1987) Heat transfer from a rotating cone or disk to fluids at any Prandtl number. *Int Commun Heat Mass Transfer* 14(3):323–332
33. Sparrow EM, Gregg JL (1959) Heat transfer from a rotating disc to fluids at any Prandtl number. *Trans ASME J Heat Transfer* 81:249–251
34. Smith NH (1946) Exploratory investigation of laminar boundary layer oscillations on a rotating disc. *NACA Tech Note* 1227:1–21
35. Gregory N, Stuart JT, Walker WS (1955) On the stability of three-dimensional boundary layers with application to the flow due to a rotating disk. *Phil Trans Roy Soc Ser A* 248:155–199
36. Corke TC, Knasiak KF (1998) Stationary travelling cross-flow mode interactions on a rotating disk. *J Fluid Mech* 355:285–315
37. Fedorov BI, Plavnik GZ, Prokhorov IV, Zhukhovitskii LG (1976) Transitional flow conditions on a rotating disk. *J Eng Phys* 31:1448–1453
38. Jarre S, Le Gal P, Chauve MP (1996) Experimental study of rotating disk instability. I. Natural flow. *Phys Fluids* 8(2):496–508
39. Jarre S, Le Gal P, Chauve MP (1996) Experimental study of rotating disk instability II. Forced flow. *Phys Fluids* 8(11):2985–2994
40. Malik MR, Wilkinson SP, Orzag SA (1981) Instability and transition in a rotating disc. *AIAA J* 19(9):1131–1138

41. Wilkinson SP, Malik MR (1985) Stability experiments in the flow over a rotating disk. *AIAA J* 23(4):588–595
42. Chin D, Litt M (1972) An electrochemical study of flow instability on rotating disk. *J Fluid Mech* 54:613–625
43. Cochran WG (1934) The flow due to a rotating disk. In: *Proceedings of Cambridge philosophical society*, vol 30, pp 365–375
44. Cooper AJ, Carpenter PW (1997) The stability of rotating-disc boundary-layer flow over a compliant wall. Part 1. Type I and II instabilities. *J Fluid Mech* 350:231–259
45. Hall P (1986) An asymptotic investigation of the stationary modes of instability of the boundary layer on a rotating disk. In: *Proceedings of royal society of London A*, vol 406, no 1830, pp 93–106
46. Kohama Y (1983) Study on boundary layer transition of a rotating disk. *Acta Mech* 50(3–4):193–199
47. Lingwood RJ (1995) Absolute instability of the boundary layer on a rotating disk. *J Fluid Mech* 299:17–33
48. Lingwood RJ (1997) Absolute instability of the Ekman layer and related rotating flows. *J Fluid Mech* 331:405–428
49. Malik MR (1986) The neutral curve for stationary disturbances in rotating-disk flow. *J Fluid Mech* 164:275–287
50. Ong CL, Owen JM (1991) Computation of the flow and heat transfer due to a rotating disc. *Int J Heat Fluid Flow* 12(2):106–115
51. Pier B (2003) Finite-amplitude crossflow vortices, secondary instability and transition in the rotating-disk boundary layer. *J Fluid Mech* 487:315–343
52. Sahin I (1988) Applications of various coordinate transformations for rotating disk flow stability. *AIAA J* 26(3):368–370
53. Szeri AZ, Giron A (1984) Stability of flow over a rotating disk. *Int J Numer Methods Fluids* 4(10):989–996
54. Watanabe T (1985) Stability of boundary layers along a rotating disk. *Trans JSME Ser B* 51(470):3344–3347
55. Isachenko VP, Osipova VA, Sukomel AS (1977) *Heat transfer*. Mir Publishers, Moscow, USSR
56. Kobayashi R, Kohama Y, Takamadate Ch (1980) Spiral vortices in boundary layer transition regime on a rotating disk. *Acta Mech* 35(1–2):71–82
57. Zoueshtiagh F, Ali R, Cooley AJ, Thomas PJ, Carpenter PW (2003) Laminar-turbulent boundary-layer transition over a rough rotating disk. *Phys Fluids* 15(8):2441–2444
58. Watanabe T (1989) Effect of surface roughness on boundary layer transition on a rotating disk. *Trans JSME Ser B* 55(515):1842–1846
59. Gregory N, Walker WS (1960) Experiments on the effect of suction on the flow due to a rotating disk. *J Fluid Mech* 9:225–234
60. Clarkson MH, Chin SC, Shacter P (1980) Flow visualization of inflexional instabilities on a rotating disk. *AIAA* 80–0279:1–14
61. Dennis RW, Newstead C, Ede AJ (1970) The heat transfer from a rotating disc in an air crossflow. In: *Proceedings of IV IHTC*, vol 3. Paper no FC 7.1, Paris-Versailles, France
62. Trinkl CM, Bardas U, Weyck A, aus der Wiesche S (2011) Experimental study of the convective heat transfer from a rotating disc subjected to forced air streams. *Int J Thermal Sci* 50(1):73–80
63. Pellé J, Harmand S (2007) Heat transfer study in a discoidal system: the influence of an impinging jet and rotation. *Experim Heat Transfer* 20(4):337–358
64. Tien CL, Campbell DT (1963) Heat and mass transfer from rotating cones. *J Fluid Mech* 17:105–112
65. Daguene M (1968) Etude du transport de matière en solution, à l'aide des électrodes a disque et a anneau tournants. *Int J Heat Mass Transfer* 11(11):1581–1596
66. Dossenbach O (1976) Simultaneous laminar and turbulent mass transfer at a rotating disk electrode. *Berichte der Bunsen-Gesellschaft Phys Chem Chem Phys* 80(4):341–343

67. Mohr CM, Newman J (1976) Mass transfer to a rotating disk in transitional flow. *J Electrochem Soc* 123(11):1687–1691
68. Deslouis C, Tribollet B, Viet L (1980) Local and overall mass transfer rates to a rotating disk in turbulent and transition flows. *Electrochim Acta* 25(8):1027–1032
69. Le Palec G (1989) Numerical study of convective heat transfer over a rotating rough disk with uniform wall temperature. *Int Commun Heat Mass Transfer* 16(1):107–113
70. Le Palec G, Nardin P, Rondot P (1990) Study of laminar heat transfer over a sinusoidal—shaped rotating disk. *Int J Heat Mass Transfer* 33(6):1183–1192
71. von Karman Th (1921) Über laminare und turbulente Reibung. *Z Angew Math Mech* 1 (4):233–252
72. Cham T-S, Head TR (1969) Turbulent boundary-layer flow on a rotating disk. *J Fluid Mech* 37(1):129–147
73. Shvets IT, Dyban EP (1974) Air cooling of gas turbine parts. *Naukova Dumka, Kiev, Ukraine* (in Russian)
74. Shevchuk IV, Khalatov AA (1997) Integral method for calculating the characteristics of a turbulent boundary layer on a rotating disk: quadratic approximation of the tangent of the flow swirl angle. *Heat Transfer Res* 28(4–6):402–413
75. Shevchuk IV (1999) Simulation of heat transfer and hydrodynamics over a free rotating disk using an improved radial velocity profile. *J Thermal Sci* 8(4):243–249
76. Abrahamson S, Lonnes S (1993) An integral method for turbulent boundary layers on rotating disks. *Trans ASME J Fluids Eng* 115(4):614–619
77. Kapinos VM (1964) Hydraulic resistance and heat transfer of a free disc with a cob. *Izvestiya vuzov Energetika* 11:85–92 (in Russian)
78. Case P (1966) Measurements of entrainment by a free rotating disk. *J Roy Aero Soc* 71:124–129
79. Kabkov VIa (1974) Characteristics of turbulent boundary-layer on a smooth disk rotating in a large volume. *Teplofizika i Teplotekhnika Naukova Dumka Kiev* 28:119–124 (in Russian)
80. Goldstein S (1935) On the resistance to the rotation of a disc immersed in a fluid. *Proc Cambridge Phil Soc* 31:232–241
81. Buznik VM, Artemov GA, Bandura VN, Kardashev YD, Fedorovskiy AM (1966) Heat transfer of a flat disk rotating in quiescent environment, *Izvestiya vuzov. Energetika* 1:84–86 (in Russian)
82. Kuznetsov AL (1962) Experimental investigation of heat transfer from a disk rotating in quiescent environment. *Trudy Leningrad Korablestroit Inst* 38:183–186. (in Russian)
83. Nikitenko NI (1963) Experimental investigation of heat exchange of a disk and a screen. *J Eng Phys* 6(6):1–11
84. McComas ST, Hartnett JP (1970) Temperature profiles and heat transfer associated with a single disc rotating in still air. In: *Proceedings of IV IHTC, vol 3. Paper FC 7.7, Paris-Versailles, France*
85. Tadros SE, Erian FF (1983) Heat and momentum transfer in the turbulent boundary layer near a rotating disk. *Paper ASME 83-WA/HT-6*
86. Northrop A, Owen JM (1988) Heat transfer measurements in rotating-disc systems. Part 1: The free disc. *Int J Heat Fluid Flow* 9(1):19–26
87. Northrop A (1984) Heat transfer in a cylindrical rotating cavity. D. Phil. thesis. University of Sussex, Brighton, UK
88. Johnson MC (1980) Turbulent heat transfer to a rotating disk: a review and extension of Dorfman. *Trans ASME J Heat Transfer* 102(4):780–781
89. Shevchuk IV (1998) Simulation of heat transfer in a rotating disk: the effect of approximation of the tangent of the angle of flow swirling. *High Temp* 36(3):522–524
90. Cebeci T, Bradshaw P (1984) *Physical and computational aspects of convective heat transfer*. Springer, Berlin, Heidelberg
91. Shevchuk IV (2002) Numerical modeling of turbulent heat transfer in a rotating disk at arbitrary distribution of the wall temperature. *J Eng Phys Thermophys* 75(4):885–888

92. Shevchuk IV, Saniei N, Yan XT (2001) Effect of the wall temperature distribution in direct and inverse problems of laminar heat transfer over a free rotating disk. In: Proceedings of 35th ASME NHTC'01. Paper NHTC2001-20196, Anaheim, California, USA
93. Shevchuk IV (2001) Turbulent heat transfer over a free rotating disk: analytical and numerical predictions using solutions of direct and inverse problems. In: Proceedings of IMECE'01. New York, USA, pp 1-8
94. Saniei N, Yan X (1998) Effect of jet location on impingement cooling of a rotating disk. Proc ASME HTD 361:203-210
95. Saniei N, Yan XT, Schooley WW (1998) Local heat transfer characteristics of a rotating disk under jet impingement cooling. Proc 11th IHTC Heat Transfer 5:445-450
96. Saniei N, Yan XT (2000) An experimental study of heat transfer from a disk rotating in an infinite environment including heat transfer enhancement by jet impingement cooling. J Enhanced Heat Transfer 7:231-245
97. Shevchuk IV (2005) A new type of the boundary condition allowing analytical solution of the thermal boundary layer equation. Int J Thermal Sci 44(4):374-381
98. Baughn JW, Ireland PT, Jones TV, Saniei N (1989) A comparison of the transient and heated-coating methods for measurement of local heat transfer coefficients on pin fin. Trans ASME J Heat Transfer 111(4):877-881
99. Harmand S, Pellé J, Poncet S, Shevchuk IV (2013) Review of fluid flow and convective heat transfer within rotating disk cavities with impinging jet. Int J Thermal Sci 67:1-30
100. Holman JP (1981) Heat transfer. McGraw-Hill, Inc., New York
101. Kingsley-Rowe JR, Lock GD, Owen JM (2005) Transient heat transfer measurements using thermochromic liquid crystal: lateral-conduction error. Int J Heat Fluid Flow 26(2):256-263
102. Lock GD, Daguze F, Syson BJ, Owen JM (1996) The application of thermal imaging techniques to determine heat transfer coefficients for slow thermal transients. In: Proceedings of 13th Symposium measuring techniques transonic supersonic flows in Cascades and Turbomach. Zurich, Switzerland, pp 1-7
103. Martinez-Botaz RF, Lock GD, Jones TV (1994) Heat transfer measurements in an annular cascade of transonic gas turbine blades using the transient liquid crystal technique. ASME Paper 94-GT-172, pp 1-8
104. Roy RP, Xu G, Feng J (2001) A study of convective heat transfer in a model rotor-stator disk cavity. Trans ASME J Turbomach 123(3):621-632
105. Wagner G, Kotulla M, Ott P, Weigand B, von Wolfersdorf J (2005) The transient liquid crystal technique: influence of surface curvature and finite wall thickness. Trans ASME J Turbomach 127(1):175-182
106. Luikov AV (1968) Analytical heat diffusion theory. Academic Press, New York
107. Shevchuk IV (2004) Unsteady-state laminar heat transfer in a rotating disk: self-similar solution. High Temp 42(4):592-595
108. Shevchuk IV (2006) Unsteady conjugate laminar heat transfer of a rotating non-uniformly heated disk: application to the transient experimental technique. Int J Heat Mass Transfer 49 (19-20):3530-3537
109. Schultz DL, Jones TV (1973) Heat transfer measurements in short duration hypersonic facilities. Aeronautical RD AGARDOGRAPH, NATO Advisory Group, p 165
110. Vogel G, Weigand B (2001) A new evaluation method for transient liquid crystal experiments. In: Proceedings 35th ASME NHTC'01. Paper NHTC2001-20250, Anaheim, California, USA
111. Shevchuk IV, Indinger T (2005) Transient conjugate heat transfer of a disk rotating in still air. In: Proceedings 4th international conference computational heat mass transfer. Paper ICCHMT'05-150, Paris, France
112. Weisstein EW (2002) Hypergeometric function. MathWorld. A Wolfram Web Resource